



**HAL**  
open science

# Uncertainty quantification in computational stochastic multiscale analysis of nonlinear elastic materials

Alexandre Clément, Christian Soize, Julien Yvonnet

► **To cite this version:**

Alexandre Clément, Christian Soize, Julien Yvonnet. Uncertainty quantification in computational stochastic multiscale analysis of nonlinear elastic materials. *Computer Methods in Applied Mechanics and Engineering*, 2013, 254 (-), pp.61-82. 10.1016/j.cma.2012.10.016 . hal-00749582

**HAL Id: hal-00749582**

**<https://hal.science/hal-00749582>**

Submitted on 7 Nov 2012

**HAL** is a multi-disciplinary open access archive for the deposit and dissemination of scientific research documents, whether they are published or not. The documents may come from teaching and research institutions in France or abroad, or from public or private research centers.

L'archive ouverte pluridisciplinaire **HAL**, est destinée au dépôt et à la diffusion de documents scientifiques de niveau recherche, publiés ou non, émanant des établissements d'enseignement et de recherche français ou étrangers, des laboratoires publics ou privés.

# Uncertainty quantification in computational stochastic multiscale analysis of nonlinear elastic materials

A. Clément, C. Soize\*, J. Yvonnet

*Université Paris-Est, Laboratoire Modélisation et Simulation Multi Echelle, MSME UMR  
8208 CNRS, 5 Bd Descartes, 77454 Marne-la-Vallée, France*

---

## Abstract

This paper is devoted to a computational stochastic multiscale analysis of nonlinear structures made up of heterogeneous hyperelastic materials. At the microscale level, the nonlinear constitutive equation of the material is characterized by a stochastic potential for which a polynomial chaos representation is used. The geometry of the microstructure is random and characterized by a high number of random parameters. The method is based on a deterministic non-concurrent multiscale approach devoted to micro-macro nonlinear mechanics which leads us to characterize the nonlinear constitutive equation with an explicit continuous form of the strain energy density function with respect to the large scale Cauchy Green strain states. To overcome the curse of dimensionality, due to the high number of involved random variables, the problem is transformed into another one consisting in identifying the potential on a polynomial chaos expansion. Several strategies, based on novel algorithms dedicated to high stochastic dimension, are used and adapted for the class of multi-modal random variables which may characterize the potential. Numerical examples, at both small and large scales, allow analyzing the efficiency of the approach through comparisons with classical methods.

*Keywords:* , Uncertainty quantification, Multiscale, Nonlinear materials, Computational stochastic mechanics, Nonlinear composites, Hyperelasticity

---

---

\*christian.soize@univ-paris-est.fr

## 1. Introduction

The problem of the stochastic nonlinear homogenization of heterogeneous random microstructures is a difficult task. Among the many issues related to this objective, the first ones appears at the deterministic level, where, unlike the linear case, the general form of the constitutive equations is unknown. Moreover, the principle of superposition is no longer available and makes unsuitable any analytical homogenization scheme applied to the small elastic strains. Many recent works have been devoted to overcome these difficulties and can be classified in two distinct families. First, approaches based on the extension of classical analytical homogenization methods [8, 1] and on second-order homogenization techniques [34, 26] both leading to determine the effective constitutive laws of nonlinear composites. Secondly, approaches based on numerical multiscale simulations such as concurrent methods [37, 12, 46, 49, 28] and non-concurrent ones [33, 44, 45, 50].

On the other hand, the uncertain nature at the microscopic level of many classes of heterogeneous materials, should be taken into account if one seeks to obtain a reliable model of the effective constitutive law. Thus, many recent works have been devoted to the construction and the identification of stochastic models at the finest scale and to their incorporation in a multiscale analysis through *ad hoc* numerical methods (see [48, 19] for instance). Naturally, at the present time, the different proposed approaches are only available in the case of linear elasticity and still need further developments to incorporate mechanical nonlinearities at the microscopic level. Moreover, these methods involve very high computational times, especially if one deterministic simulation appears expensive. A great challenge thus comes from the extension of the deterministic methods stated above to the stochastic framework with reasonable computational costs.

Based on a novel efficient non-concurrent multiscale approach developed by Yvonnet and coworkers [50, 51, 52], we have extended this method to the stochastic case in [7]. The so-called Stochastic Numerical EXplicit Potentials method (S-NEXP) aims at numerically determine the apparent strain energy density function according to the large scale strain states and the random variables describing the uncertainties related to the microstructure (geometrical or material parameters). This parametric technique allows one getting efficient solutions but suffers from the “curse of dimensionality” since the interpolation scheme requires a high number of microscopic nonlinear numerical simulations. This problem is similar to the one encountered in

the framework of stochastic intrusive techniques, such as Galerkin methods which rely on conventional tensor-product integration rules. However, taking into account a high number of random parameters is of first importance in a stochastic multiscale analysis and we thus propose a different methodology based on polynomial chaos representations. Initiated in [14], the methodology to construct a polynomial chaos expansion of random fields has been intensely developed to solve stochastic partial differential equations [3, 15, 16, 13, 24, 22, 29, 32, 31, 35, 38, 11] but also for the identification of random fields using experimental data and classical inference techniques [17, 2] or maximum likelihood estimation [9, 10, 43, 18]. A new methodology has been recently introduced to deal with the identification of polynomial chaos representations in high-dimension [39, 41]. We propose to use this novel technique in order to obtain a representation of the stochastic nonlinear constitutive equations which can thus be seen as a stochastic non-intrusive technique as opposed to the Stochastic Numerical EXplicit Potentials method [7] which suffers from the classical tensor-product interpolation rules since it acts as an intrusive technique. Then, we based our approach on the same nonlinear homogenization scheme presented in [7] but the methodology proposed to characterize the stochastic apparent nonlinear constitutive equations is totally different. Indeed, we use the NEXP approach [52] as a deterministic solver, which is not directly extended to the stochastic framework, and we reformulate the problem into the identification of polynomial chaos expansions in high-dimension.

The paper is organized as follows. Section 2 deals with the homogenization of nonlinear heterogeneous materials at finite strains in a deterministic framework. In the same section, the Numerical EXplicit Potentials method (NEXP) is also briefly presented. Section 3 presents the probabilistic model which allows generating realizations of the microstructure. In Section 4, we then detail the procedure of identification of the reduced-order random variables, resulting from a principal component analysis, on polynomial chaos expansions. Since the problem of identifying multi-modal random variables arises, we define a prior stochastic model based on mixtures of polynomial chaos as introduced in [30]. Both cases of uni-modal and multi-modal random variables are then addressed. The efficiency of the proposed method is shown in Section 6 with two numerical examples at the microscale and one example at the mesoscale. For each problem, the proposed approach is compared with classical methods showing its efficiency. Some concluding remarks are finally drawn in Section 7.

## 2. The method of Numerical EXplicit Potentials

In this section, we detail the nonlinear homogenization scheme applied to hyperelastic heterogeneous materials and we present the deterministic method of Numerical EXplicit Potentials [50, 51, 52, 7] (NEXP) leading to a continuous explicit form of the strain energy density function which characterizes the effective constitutive equations. In the field of homogenization, knowledge on the separation of the scales is vital to perform an appropriate mechanical analysis. We set apart two cases: the case where the two scales are the microscale and the macroscale and the case for which the two scales are the microscale and the mesoscale. More precisely, when the two considered scales are the microscale and the macroscale, the scales are separated. Such a separation is obtained when the spatial correlation lengths of the mechanical fields at the microscale are small enough with respect to the macroscale. The statistical fluctuations at the macroscale are then negligible and the macroscopic mechanical quantities are thus deterministic and are referred as the effective properties. On the other hand, when the two considered scales are the microscale and the mesoscale, the scales are not separated. The statistical fluctuations at the mesoscale are important and the mesoscopic mechanical quantities are stochastic and referred as the apparent properties. The proposed method can be used in both cases, as it will be shown in the numerical examples. Then, in order to simplify the writing of this paper without loss of generality, we use the following terminology. The small scale indicates the microscale and the large scale indicates either the macroscale or the mesoscale. Moreover, both the effective quantities, linked to the macroscale, and the apparent quantities, linked to the mesoscale, are referred as the apparent quantities.

### 2.1. Nonlinear homogenization scheme

We consider a microstructure, schematically depicted on figure 1, which occupies a domain  $\Omega \subset \mathbb{R}^d$  where  $d \in \{1, 2, 3\}$  denotes the spatial dimension and where  $\partial\Omega$  denotes the boundary of the domain  $\Omega$ . We identify the position of the material points by the vector  $\mathbf{X}$  in the reference configuration and by  $\mathbf{x}$  in the deformed configuration. Those two vectors are related through:

$$\mathbf{x} = \mathbf{X} + \mathbf{u}, \quad (1)$$

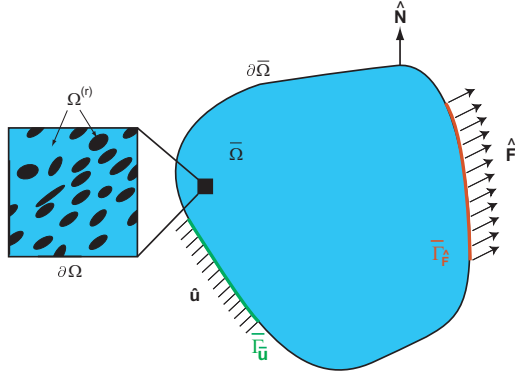


Figure 1: Model problem: small scale and large scale structures.

where  $\mathbf{u}$  is the displacement vector of a material point. We introduce the deformation gradient tensor  $\mathbf{F}$  at point  $\mathbf{X}$  defined by

$$\mathbf{F} = \frac{\partial \mathbf{x}}{\partial \mathbf{X}} = \mathbf{1} + \nabla_{\mathbf{X}}(\mathbf{u}), \quad (2)$$

where  $\mathbf{1}$  is the second-order identity tensor and  $\nabla_{\mathbf{X}}(\cdot)$  is the gradient operator according to the reference configuration. Domain  $\Omega$ , characterizing the microstructure, is composed of  $N_p$  hyperelastic phases defining the  $N_p$  domains  $\Omega^{(r)}$  with  $r \in \{1, \dots, N_p\}$  and such that  $\Omega = \bigcup_{r=1}^{N_p} \Omega^{(r)}$ . The constitutive equations of each phase can then be characterized by strain energy density functions  $\psi^{(r)}$  according to the right-hand Cauchy-Green strain tensor  $\mathbf{C} = \mathbf{F}^T \mathbf{F}$  such that the local strain energy density function  $\psi$  of  $\Omega$  can be written as

$$\psi(\mathbf{X}, \mathbf{C}) = \sum_{r=1}^{N_p} \mathbb{I}^{(r)}(\mathbf{X}) \psi^{(r)}(\mathbf{C}), \quad (3)$$

where  $\mathbb{I}^{(r)}$  is the characteristic function of domain  $\Omega^{(r)}$  which is equal to 1 if  $\mathbf{X} \in \Omega^{(r)}$  and 0 otherwise. Let us denote by  $\mathbf{P}$  and  $\mathbf{S}$  the first and second Piola-Kirchhoff stress tensors respectively, related by  $\mathbf{P} = \mathbf{F} \mathbf{S}$ . In the Lagrangian description, the local constitutive equation is given by (see *e.g.* [20])

$$\mathbf{S} = 2 \frac{\partial \psi}{\partial \mathbf{C}}(\mathbf{X}, \mathbf{C}). \quad (4)$$

In the present work, we consider a compressible Neo-Hookean model (see [20] for instance) described by the following potential

$$\psi(\mathbf{C}) = \frac{1}{2}\lambda\{\log(J)\}^2 - \mu\log(J) + \frac{1}{2}\mu(\text{tr}(\mathbf{C}) - 3), \quad (5)$$

where  $\log(\cdot)$  indicates the natural logarithm,  $J = \det(\mathbf{F})$  is the volumetric change,  $\lambda = \frac{E\nu}{(1+\nu)(1-2\nu)}$  and  $\mu = \frac{E}{2(1+\nu)}$  in which  $E$  and  $\nu$  are respectively the Young modulus and the Poisson ratio. We also introduce the fourth-order tangent elastic tensor  $\mathbf{L}$  defined by

$$\mathbf{L} = 4\frac{\partial^2\psi(\mathbf{X}, \mathbf{C})}{\partial\mathbf{C}^2}. \quad (6)$$

The apparent (or effective) kinematic quantities are defined by volume averaging on the elementary cell as

$$\overline{\mathbf{F}} = \langle \mathbf{F} \rangle, \quad (7)$$

$$\overline{\mathbf{C}} = \overline{\mathbf{F}^T \mathbf{F}} \neq \langle \mathbf{C} \rangle, \quad (8)$$

and the following apparent strains tensors

$$\overline{\mathbf{P}} = \langle \mathbf{P} \rangle, \quad (9)$$

$$\overline{\mathbf{S}} = \overline{\mathbf{F}^{-1} \mathbf{P}} \neq \langle \mathbf{S} \rangle, \quad (10)$$

where the symbol  $\langle \cdot \rangle$  denotes the spatial averaging over  $\Omega$ . Using equations (7) to (10), it can be shown (see a proof in [52]):

$$\overline{\mathbf{S}} = 2\frac{\partial\overline{\psi}(\overline{\mathbf{C}})}{\partial\overline{\mathbf{C}}}, \quad (11)$$

$$\overline{\mathbf{L}} = 4\frac{\partial^2\overline{\psi}(\overline{\mathbf{C}})}{\partial\overline{\mathbf{C}}^2}, \quad (12)$$

where  $\overline{\psi}(\overline{\mathbf{C}})$  is the apparent (or effective) strain energy density function. Thus, for a given large scale strain state  $\overline{\mathbf{C}}$ , the corresponding value of  $\overline{\psi}(\overline{\mathbf{C}})$  is determined by taking the spatial average of local strain energy density functions  $\psi(\mathbf{X}, \mathbf{C})$ , where  $\mathbf{C}(\mathbf{X})$  is the strain field at equilibrium. The involved nonlinear mechanical problems which must satisfy the local equilibrium condition at each scale are detailed in [52, 7]. They are classically linearized and solved with the Finite Element Method (FEM).

## 2.2. The method of Numerical EXplicit Potentials

The NEXP method aims at numerically determine the strain energy density function  $\bar{\psi}(\bar{\mathbf{C}})$  for a finite set of large scale boundary conditions depending on tensor  $\bar{\mathbf{C}}$ . The resulting values are then used to calculate an efficient separated variables representation of the potential whose coefficients are interpolated according to  $\bar{\mathbf{C}}$ . The components of apparent tensors  $\bar{\mathbf{S}}(\bar{\mathbf{C}})$  and  $\bar{\mathbf{L}}(\bar{\mathbf{C}})$ , required to solve the large scale problem, can thus be obtained by derivation of the apparent strain energy density function.

The main steps of the approach are summarized as follows.

1. Defining an elementary cell representing the microstructure of the heterogeneous material.
2. Defining and discretizing the bounded space  $\Delta_{\bar{\mathbf{C}}}$  spanned by the large scale (mesoscopic or macroscopic) strains related to the components of the right Cauchy-Green strain tensor  $\bar{\mathbf{C}}$  into a finite number  $p$  of nodes.
3. Computing the apparent (or effective) strain energy density function  $\bar{\psi}(\bar{\mathbf{C}})$  for each node of the discretized space  $\Delta_{\bar{\mathbf{C}}}$  corresponding to different boundary conditions applied on the elementary cell. The numerical data are stored in a hypermatrix  $\bar{\mathbb{W}}$ .
4. Interpolating the values of the database to obtain a continuous mapping relating the components of  $\bar{\mathbf{C}}$  to the apparent (or effective) strain energy density function  $\bar{\psi}(\bar{\mathbf{C}})$ . While different solutions exist to perform interpolation (see *e.g.* [50]), we adopt in this work a method based on a separated representation of  $\bar{\mathbb{W}}$  (see [7, 50]).

Using the notations defined in [7], similar to the Voigt ones, the continuous interpolation of  $\bar{\psi}$  can be approximated by

$$\bar{\psi} \approx \sum_{r=1}^R \prod_{k=1}^D \tilde{\phi}_k^r(\bar{\mathbf{C}}_k), \quad (13)$$

where  $\tilde{\phi}_j^r(\omega_j)$  are the interpolated values of the real-valued vectors  $\{\phi_k^r, k_1 = 1, \dots, D\}$  related to the macroscopic scale strain tensor component  $\bar{\mathbf{C}}_i$  and  $R$  is an integer. Thus, the components of the second Piola-Kirchhoff stress tensor can be approximated by

$$\bar{S}_i(\bar{\mathbf{C}}_1, \dots, \bar{\mathbf{C}}_D) \approx 2 \sum_{r=1}^R \left( \left\{ \prod_{k \neq i} \tilde{\phi}_k^r(\bar{\mathbf{C}}_k) \right\} \frac{\partial \tilde{\phi}_i^r(\bar{\mathbf{C}}_i)}{\partial \bar{\mathbf{C}}_i} \right), \quad (14)$$

in which  $k = 1, \dots, D$ . In the same manner, the components of tangent elastic tensor  $\bar{\mathbf{L}}$  can be approximated by

$$\bar{L}_{ij} \approx 4 \gamma_{ij} \sum_{r=1}^R \left( \left\{ \prod_{k \neq i, j} \tilde{\phi}_k^r(\bar{C}_k) \right\} \frac{\partial \tilde{\phi}_i^r(\bar{C}_i)}{\partial \bar{C}_i} \frac{\partial \tilde{\phi}_j^r(\bar{C}_j)}{\partial \bar{C}_j} \right) \text{ if } i \neq j, \quad (15)$$

$$\bar{L}_{ii} \approx 4 \gamma_{ii} \sum_{r=1}^R \left( \left\{ \prod_{k \neq i} \tilde{\phi}_k^r(\bar{C}_k) \right\} \frac{\partial^2 \tilde{\phi}_i^r(\bar{C}_i)}{\partial \bar{C}_i^2} \right), \quad (16)$$

The interpolation functions are chosen as one-dimensional  $\mathcal{C}^2$  cubic spline functions (see [50, 52]) for which results of convergence with respect to the number of discretization points have been studied. However, one should note that many other choices are available.

### 3. Probabilistic model and random generator of geometries of the microstructure

This work is focussed on heterogeneous materials for which the geometrical parameters characterizing the microstructure are random. In particular, we are interested in composites made of polymer matrix and reinforced by non penetrating long fibers. The geometrical modeling of the fibers is depicted on figure 2. One fiber is represented by an ellipse parametrized by 5 constants: the horizontal and vertical positions  $X$  and  $Y$  of its center, an aspect ratio  $\alpha$ , the length of its semi-major axis  $a$  and its orientation angle  $\gamma$  according to vector  $\mathbf{e}_3$ . Introducing the semi-minor axis  $b$ , the aspect ratio  $\alpha$  is defined by  $\alpha = b/a$  with  $\alpha \in ]0, 1]$ . We also introduce the number of fibers  $N_f$  composing the geometry of the microstructure which yields a number  $N = 5N_f$  of geometrical parameters. Since the condition of impenetrability of the fibers is a key point in the model, we propose to generate a greater number  $n \gg N_f$  of “possible” geometrical parameters. Then, the verification of the impenetrability condition will act as a rejection process. We here adopt a parametric approach to deal with the uncertainties. We set  $m = 5n$ . The geometry is modeled by a  $\mathbb{R}^m$ - valued random variable with probability distribution  $P_\xi$  for which its support is a subset of  $\mathbb{R}^m$ . Considering the geometrical parametrization previously introduced, the random “possible” geometrical parameters are represented by the second-order random vector

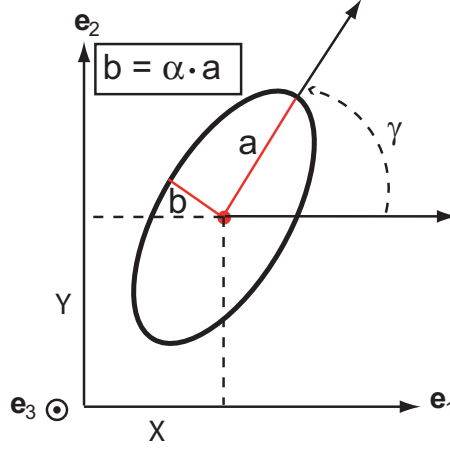


Figure 2: Geometrical description of a fiber

$\xi$  defined by

$$\begin{aligned} \xi &= (\mathbf{X}, \mathbf{Y}, \boldsymbol{\alpha}, \mathbf{a}, \gamma) \\ &= (X_1, \dots, X_n, Y_1, \dots, Y_n, \alpha_1, \dots, \alpha_n, a_1, \dots, a_n, \gamma_1, \dots, \gamma_n). \end{aligned} \quad (17)$$

Since the direct construction of  $P_\xi$  is not a trivial task, we use a random generator similar to the one proposed in [7]. The aim is to generate the independent realizations  $\{\mathbf{X}^{(k)}\}_{k=1}^\nu$ ,  $\{\mathbf{Y}^{(k)}\}_{k=1}^\nu$ ,  $\{\boldsymbol{\alpha}^{(k)}\}_{k=1}^\nu$ ,  $\{\mathbf{a}^{(k)}\}_{k=1}^\nu$  and  $\{\gamma^{(k)}\}_{k=1}^\nu$  which characterize the random vectors  $\mathbf{X}$ ,  $\mathbf{Y}$ ,  $\boldsymbol{\alpha}$ ,  $\mathbf{a}$  and  $\gamma$ , yielding the independent realizations  $\{\xi^{(k)}\}_{k=1}^\nu$  of random vector  $\xi$ . The realizations of each random vector  $\mathbf{X}$ ,  $\mathbf{Y}$ ,  $\boldsymbol{\alpha}$ ,  $\mathbf{a}$  and  $\gamma$  are generated through the same procedure with different or identical input parameters including a spatial correlation parameter  $\rho$  and a coefficient of variation  $\delta$ . This procedure is completely detailed in [7]. Once the set of realizations  $\{\xi^{(k)}\}_{k=1}^\nu$  is computed, the final step for obtaining the geometry of the microstructure consists in a selection of the realizations verifying the condition of impenetrability of the fibers leading to the new set of realizations  $\{\xi^{(k)}\}_{k=1}^\mu$  with  $\mu \leq \nu$ . One must note that the random generator characterizing the probabilistic model can be replaced by any other random generator with the same capabilities in order to model more complex shapes or arbitrary shapes.

#### 4. Identification of a high-dimension polynomial chaos expansion of the apparent strain energy density function

The central idea of the proposed approach is to obtain a continuous explicit form of the strain energy density function  $\bar{\psi}$  which characterizes the apparent (or effective) constitutive behavior of the material depending on random parameters. The main idea is to determine a polynomial chaos expansion of a discretized  $\bar{\psi}$  according to a finite set of large scale (mesoscopic or macroscopic) boundary conditions depending on tensor  $\bar{\mathbf{C}}$ . With such a form, the separated variables representation defined by Eq. (13) associated with the interpolation scheme presented in Section 2, will be used as post-processing to determine the continuous explicit form of  $\bar{\psi}(\bar{\mathbf{C}})$  for a particular geometry of the microstructure. We propose to determine a polynomial chaos expansion of each component of hypermatrix  $\bar{\mathbb{W}}$  and thus of the apparent (or effective) potential. Since the geometry or the microstructure is random, the local potential  $\psi(\mathbf{X}, \mathbf{C})$  is also random and defined by a stochastic local potential such as

$$\Psi(\mathbf{X}, \mathbf{C}) := \psi(\mathbf{X}, \mathbf{C}, \boldsymbol{\xi}). \quad (18)$$

The apparent strain energy density function is thus obtained by volume averaging of the stochastic local potential such as

$$\bar{\Psi}(\bar{\mathbf{C}}) = \langle \Psi(\mathbf{X}, \mathbf{C}) \rangle_{\mathbf{X}}, \quad (19)$$

where  $\bar{\Psi}(\bar{\mathbf{C}})$  is a  $\mathbb{R}$ -valued random variable. Since the apparent Cauchy-Green strain tensor is discretized into a finite number of nodes  $\{\bar{\mathbf{C}}_i\}_{i=1}^Q$ , the apparent potential is characterized by a  $\mathbb{R}^Q$ -valued random vector  $\bar{\Psi}(\bar{\mathbf{C}})$  defined by

$$\bar{\Psi}(\bar{\mathbf{C}}) = (\bar{\Psi}(\bar{\mathbf{C}}_1), \dots, \bar{\Psi}(\bar{\mathbf{C}}_Q)), \quad (20)$$

where integer  $Q$  indicates the number of components of  $\bar{\mathbb{W}}$ . Below, for notational convenience, the components  $\bar{\Psi}(\bar{\mathbf{C}}_i)$  are simply denoted by  $\bar{\Psi}_i$ . Then, each component  $\{\bar{\Psi}_i, i = 1, \dots, Q\}$  of  $\bar{\Psi}$  corresponds to the value of  $\bar{\Psi}$  for a particular value of the apparent right-hand Cauchy-Green strain tensor  $\bar{\mathbf{C}}$  corresponding to a discretized node of domain  $\Delta_{\bar{\mathbf{C}}}$ .

In 3 we have proposed a random generator which allows obtaining a finite set  $\{\boldsymbol{\xi}^{(k)}\}_{k=1}^{\mu}$  of independent realizations of the geometry of the microstructure. For each realization  $\boldsymbol{\xi}^{(k)}$ , the vector  $\bar{\Psi}(\bar{\mathbf{C}})$  is computed, using the Numerical EXplicit Potentials method, and yields a set of realizations  $\{\bar{\Psi}^{(k)}\}_{k=1}^{\mu}$ .

This set of realizations of the discretized strain energy density function is the starting point of the approach and will be referred as the numerical data. The next step consists in defining a stochastic model of  $\overline{\Psi}$  based on representations on polynomial chaos expansions. The methodology used to construct a polynomial chaos expansion [14, 23] of  $\overline{\Psi}$  is the one presented in [39, 41] for the high dimensional stochastic case and consists here (a) in reducing the random vector  $\overline{\Psi}$  with a principal component analysis and then (b) in identifying the polynomial chaos expansion of the reduced-order random variables in terms of the length  $N_g$  of the germ, the maximum degree  $N_d$  of the polynomial chaos and the vector-valued deterministic coefficients of the expansions. The procedure is summarized in the following section.

#### 4.1. Summarizing the identification of a high-dimension polynomial chaos expansion

Using a principal component analysis, the  $\mathbb{R}^Q$ -valued random vector  $\overline{\Psi}$ , characterized by the set of realizations  $\{\overline{\Psi}^{(k)}\}_{k=1}^\mu$ , is written as follows

$$\overline{\Psi} \simeq \boldsymbol{\mu}_{\overline{\Psi}} + \sum_{j=1}^M \sqrt{\lambda_j} \boldsymbol{\varphi}_j \zeta_j, \quad (21)$$

in which  $\boldsymbol{\mu}_{\overline{\Psi}} = \mathbb{E}\{\overline{\Psi}\}$  and  $\{\lambda_j, \boldsymbol{\varphi}_j\}_{j=1}^M$  are the  $M$  first largest eigenvalues and associated eigenvectors of the covariance matrix of random vector  $\overline{\Psi}$ . Second-order random variables  $\zeta_1, \dots, \zeta_M$  are centered and orthonormal, that is to say,  $\mathbb{E}\{\zeta_j\} = 0$  and  $\mathbb{E}\{\zeta_j \zeta_{j'}\} = \delta_{jj'}$ . Integer  $M$  is assumed to be sufficiently large to reach the mean-square convergence which is controlled by

$$\sqrt{1 - \frac{\sum_{j=1}^M \lambda_j}{\text{tr}[\mathbf{C}_{\overline{\Psi}}]}} = \epsilon_{KL}^M < \epsilon_{KL}, \quad (22)$$

in which  $\epsilon_{KL}$  is the tolerance parameter. The random vector  $\overline{\Psi}$  is characterized by the set of realizations  $\{\overline{\Psi}^{(k)}\}_{k=1}^\mu$ . Introducing the vector  $\boldsymbol{\zeta}^{(k)} = (\zeta_1^{(k)}, \dots, \zeta_M^{(k)})$ , we deduce that  $\{\boldsymbol{\zeta}^{(k)}\}_{k=1}^\mu$  are the independent realizations of random vector  $\boldsymbol{\zeta}$ , which represents the strain energy density function for the prescribed large scale strain states, given by

$$\zeta_j^{(k)} = \frac{1}{\sqrt{\lambda_j}} \boldsymbol{\varphi}_j^T (\overline{\Psi}^{(k)} - \boldsymbol{\mu}_{\overline{\Psi}}). \quad (23)$$

The reduced-order random vector  $\boldsymbol{\zeta} = (\zeta_1, \dots, \zeta_M)$ , characterized by the realizations  $\{\bar{\boldsymbol{\zeta}}^{(k)}\}_{k=1}^\mu$ , has an arbitrary probability distribution which is characterized by projecting  $\boldsymbol{\zeta}$  onto the Gaussian polynomial chaos leading to the following approximation

$$\boldsymbol{\zeta} \simeq \boldsymbol{\zeta}^{PC} = \sum_{\alpha=1}^N \mathbf{y}^\alpha H_\alpha(\boldsymbol{\Xi}), \quad (24)$$

where the real valued random variables  $H_1(\boldsymbol{\Xi}), \dots, H_N(\boldsymbol{\Xi})$  are the renumbered normalized Hermite polynomials of the  $\mathbb{R}^{N_g}$  valued normalized Gaussian random variables  $\boldsymbol{\Xi} = (\Xi_1, \dots, \Xi_{N_g})$  verifying that  $\mathbb{E}\{\boldsymbol{\Xi}\} = 0$  and  $\mathbb{E}\{\boldsymbol{\Xi}\boldsymbol{\Xi}^T\} = [I_{N_g}]$ , and where deterministic coefficients  $\mathbf{y}^1, \dots, \mathbf{y}^N$  are vectors in  $\mathbb{R}^M$  such that

$$\sum_{\alpha=1}^N \mathbf{y}^\alpha \mathbf{y}^{\alpha T} = [I_M], \quad (25)$$

with  $[I_M]$  the  $(M \times M)$  identity matrix. The realizations of orthogonal polynomials  $H_\alpha(\boldsymbol{\Xi})$  are computed with the technique proposed in [40] for the high-dimension case. This method ensures that the orthogonality properties of the polynomials  $H_\alpha(\boldsymbol{\Xi})$  are numerically satisfied (especially in high dimension) and would also be available for any arbitrary probability measure of real-valued random variables  $\boldsymbol{\Xi}$ . We denote by  $N_d$  the integer number indicating the maximum degree of the orthonormal polynomials in (24). The number  $N$  of polynomials in Eq. (24) is thus  $N = h(N_g, N_d) = (N_g + N_d)! / (N_g! N_d!)$ . The problem is thus to identify the  $N$  deterministic vector-valued coefficients  $\mathbf{y}^1, \dots, \mathbf{y}^N$  in  $\mathbb{R}^M$  which must verify Eq. (25).

The random vector  $\bar{\boldsymbol{\Psi}}$ , characterizing the apparent potential and fully defined by Eqs. (21) and (24), must be a positive-valued random vector which is naturally the case for  $N \rightarrow +\infty$  in Eq. (24). Consequently, for a fixed value of  $N$ , this condition could not be satisfied even if the mean-square convergence of the series (24) seems to be reached. However, in practice, no particular constraint is added to the problem since the numerical tests have shown that this condition was always satisfied, that is to say that no realization, generated with Eq. (24), had to be rejected.

The identification of the vector-valued coefficients  $\mathbf{y}^1, \dots, \mathbf{y}^N$  for a fixed value of  $N$  is done using the maximum likelihood method [36, 42] as performed in [2, 43, 10]. For a given value of  $\mathbf{y}^1, \dots, \mathbf{y}^N$ , the estimation of

$p_{\zeta_j^{PC(N)}}(\zeta_j^{(k)}; \mathbf{y}^1, \dots, \mathbf{y}^N)$  is performed using the kernel density estimation method [5] with the set of independent realizations  $\{\zeta^{(k)}\}_{k=1}^\mu$  calculated with Eq. (23), and using Eq. (25) and  $\mu_{PC}$  independent realizations  $\Xi(\theta_1), \dots, \Xi(\theta_{\mu_{PC}})$  of the normalized Gaussian vector  $\Xi$ .

The optimal value  $(\underline{\mathbf{y}}^1, \dots, \underline{\mathbf{y}}^N)$  of  $(\mathbf{y}^1, \dots, \mathbf{y}^N)$  is then the solution of the following optimization problem

$$(\underline{\mathbf{y}}^1, \dots, \underline{\mathbf{y}}^N) = \arg \max_{(\mathbf{y}^1, \dots, \mathbf{y}^N) \in \mathcal{C}_{ad}^N} \mathcal{L}(\mathbf{y}^1, \dots, \mathbf{y}^N), \quad (26)$$

in which admissible set  $\mathcal{C}_{ad}^N$  is such that

$$\mathcal{C}_{ad}^N = \left\{ (\mathbf{y}^1, \dots, \mathbf{y}^N) \in (\mathbb{R}^M)^N, \sum_{\alpha=1}^N \mathbf{y}^\alpha \mathbf{y}^{\alpha T} = [I_M] \right\}. \quad (27)$$

Solving this type of optimization problem, defined by Eqs. (26) and (27), on a Stiefel manifold defined by Eq. (25) is not a trivial task if one seeks to use both a high length of germ  $N_g$  and a high maximum degree  $N_d$  of the polynomial chaos. Using the methodology proposed in [39], the optimization problem defined by Eqs. (26) and (27) is reformulated into a set of recurrent optimization problems  $\mathcal{P}_1, \dots, \mathcal{P}_M$  for  $\ell = 1, \dots, M$  related to each reduced-order random variable  $\zeta_j$  and depending only on the polynomial chaos coefficients for each  $\zeta_j$ . The new optimization problems are not convex problem and they are thus solved using the algorithm proposed in [39] and also successfully employed in [41]. This algorithm consists in a two-steps random search algorithm for which  $\mu_{rs}$  realizations of the coefficients of the polynomial chaos expansions are used for each step. Its advantage mainly comes from automatically verifying the constraint defined by Eq. (25). In the various numerical examples, this strategy of identification will be referred as strategy (UM).

#### 4.2. Prior stochastic model for the identification of multi-modal random variables using mixture of polynomial chaos expansions

As it will be shown in Section 6.2, reduced-order random variables  $\{\zeta_j, j = 1, \dots, M\}$  are each characterized by marginal probability density function  $p_{\zeta_j}$  which may possess several modes, that is to say several local maxima. Classical polynomial chaos decompositions may thus require, for this particular class of random variables, a large number  $N$  of basis functions to

converge. We then propose a prior stochastic model using polynomial chaos representations based on the methodology proposed in [30] where mixture of polynomial chaos are used to represent a multi-modal scalar random variable in an efficient way. The extension of this technique to the case of vector-valued random variables is not straightforward since a high amount of realizations are required to estimate the joint probability density functions. We thus propose a prior stochastic model based on mixture of polynomial chaos which takes into account the information on the multi-modality of the marginal probability density functions  $\{p_{\zeta_j}, j = 1, \dots, M\}$ . This strategy, denoted by (MM) in the following, will be numerically tested in Sec. 6.2.

We define the number of modes  $M_j^{mode}$  of a reduced-order random variable  $\zeta_j$ , whose support is  $\mathbb{R}$ , as the number of local maxima of the probability density function  $p_{\zeta_j}$  of  $\zeta_j$ . The aim of the representation is to separate the different modes of each probability density function  $p_{\zeta_j}$  and to seek a polynomial chaos representation of each resulting uni-modal probability density function. By denoting  $S_j = \text{supp } p_{\zeta_j}$  the support of the probability density function  $p_{\zeta_j}$ , we assume that  $S_j$  is bounded such that  $S_j = [S_j^{min}, S_j^{max}]$ . We then introduce a partition of the interval  $[S_j^{min}, S_j^{max}]$  defined by intervals  $\{K_{j,i}\}_{i=1}^{M_j^{mode}}$ , verifying that  $S_j = \bigcup_{i=1}^{M_j^{mode}} K_{j,i}$  with  $\bigcap_{i=1}^{M_j^{mode}} K_{j,i} = \emptyset$ . The intervals  $\{K_{j,i}\}_{i=1}^{M_j^{mode}}$  are defined by  $K_{j,i} = [q_{i-1}, q_i)$  where  $S_j^{min} = q_0 < q_1 < \dots < q_{M_j^{mode}} = S_j^{max}$ . Separation points  $\{\delta_i\}_{i=0}^{M_j^{mode}}$ , including  $S_j^{min}$  and  $S_j^{max}$ , are estimated with probability density function computed with the kernel density estimation method given in [4] which allows determining an appropriate bandwidth to exhibit the different modes of the probability density function of the random variable  $\zeta_j$ . Then, introducing a uniform random variable  $\widehat{\Xi}_j$  on  $[S_j^{min}, S_j^{max}]$ , we can define the indicator function  $\mathbb{I}_{K_{j,i}}$  of  $K_{j,i}$  and seek a mixture of polynomial chaos representation of  $\zeta_j$  under the following form

$$\zeta_j(\widehat{\Xi}_j, \Xi) \simeq \sum_{i=1}^{M_j^{mode}} \mathbb{I}_{K_{j,i}}(\widehat{\Xi}_j) \left( \sum_{\alpha=1}^N y_{j,i}^\alpha H_\alpha(\Xi) \right), \quad (28)$$

which can be seen as a functional representation of random variable  $\zeta_j$  with respect to  $\widehat{\Xi}_j$  and  $\Xi$ . Functions  $\{\mathbb{I}_{K_{j,i}} H_\alpha\}$  form an orthogonal set of functions composed by piecewise polynomial functions which are polynomial according to  $\Xi$  and piecewise constant according to  $\widehat{\Xi}_j$ . The identification of the deterministic coefficients of the polynomial chaos expansions is done with the

technique given in [39]. This technique is used for each mode and has thus to be employed  $M_j^{mode}$  times. However, the computational times are not increased and may even be reduced since the identification of random variables with uni-modal probability density functions is fast. The performances of the proposed prior stochastic model are discussed in Sections 6.2 and 6.3.

#### 4.3. Error estimation

In order to control the quality of the convergence of the series in Eqs. (24) and (28) with respect to  $N$ , we use the specific error function introduced in [39, 41]. This unusual  $L^1$ -log error function allows the error of very small values of the probability density function to be measured. For a fixed value of  $N$ , such a measurement is summarized in the following. Let  $e \mapsto p_{\zeta_j}(e)$  be the probability density function of the random variable  $\zeta_j$ . The convergence of random vectors  $\zeta^{PC}$  towards  $\zeta$  according to  $N$  is then controlled with the  $L^1$ -log error defined by

$$err_j(N_g, N_d) = \int_{BI_j} |\log_{10} p_{\zeta_j}(e) - \log_{10} p_{\zeta_j^{PC}(N)}(e; \mathbf{y}^1, \dots, \mathbf{y}^N)| de, \quad (29)$$

where  $BI_j$  is the intersection of the bounded supports of  $e \mapsto p_{\zeta_j}(e)$  and  $e \mapsto p_{\zeta_j^{PC}(N)}(e; \mathbf{y}^1, \dots, \mathbf{y}^N)$ . The estimation of  $p_{\zeta_j}(e)$  is performed using the kernel density estimation method [5] with the set of independent realizations  $\{\zeta^{(k)}\}_{k=1}^\mu$  calculated with Eq. (23). The  $L^1$ -log error function related to the random vector  $\zeta^{PC}$  and denoted by  $err(N_g, N_d)$  is defined by

$$err(N_g, N_d) = \frac{1}{M} \sum_{j=1}^M err_j(N_g, N_d). \quad (30)$$

## 5. Summary of the overall procedure

For the sake of clarity, we summarize the overall proposed method. Thus, the main steps of the approach can be classified as follows.

1. Defining the parameters of the random generator to obtain the set of realizations  $\{\xi^{(k)}\}_{k=1}^\mu$  of the microstructure geometry.
2. Discretizing the bounded space  $\Delta_{\overline{\mathcal{C}}}$  spanned by the large scale (mesoscopic or macroscopic) strains and computing the apparent (or effective) strain energy density function according to the prescribed large

scale strains for each realization of the geometry of the microstructure. This step leads us to the set of realizations  $\{\overline{\Psi}^{(k)}\}_{k=1}^{\mu}$  of random vector  $\overline{\Psi}$ .

3. Computing the reduced-order model of the discretized potential through a principal component analysis. This step leads to the set of realizations  $\{\zeta_j^{(k)}\}_{k=1}^{\mu}$  of reduced-order random vector  $\zeta$ .
4. Identifying the reduced-order random vector  $\zeta$  on polynomial chaos expansions, leading to the following approximation  $\zeta \simeq \sum_{\alpha=1}^N \mathbf{y}^{\alpha} H_{\alpha}(\Xi)$  with  $\sum_{\alpha=1}^N \mathbf{y}^{\alpha} \mathbf{y}^{\alpha T} = [I_M]$ .
5. Computing the separated variables representation associated with an appropriate interpolation scheme in order to obtain a continuous explicit form of each realization  $\{\overline{\Psi}^{(k)}, k = 1, \dots, \mu_{PC}\}$  of the potential leading to the following approximation  $\overline{\Psi}^{(k)}(\overline{\mathbf{C}}) \approx \sum_{r=1}^R \prod_{i=1}^D \tilde{\phi}_i^r(\overline{\mathbf{C}}_i)$ .

A pseudo-algorithm of the proposed methodology is given in Algorithm 1.

```

NEXP approach;
begin
  input : Set of realizations  $\{\xi^{(k)}\}_{k=1}^\mu$ 
           Parameter  $Q$  of discretization of  $\Delta_{\overline{\mathcal{C}}}$ 
  for  $k = 1$  to  $\mu$  do
    | Compute  $\overline{\Psi}^{(k)}(\overline{\mathcal{C}}) = (\overline{\Psi}^{(k)}(\overline{\mathcal{C}}_1), \dots, \overline{\Psi}^{(k)}(\overline{\mathcal{C}}_Q))$ 
  end
  output: Set of realizations  $\{\overline{\Psi}^{(k)}\}_{k=1}^\mu$ 
end

Principal Component Analysis;
begin
  input : Set of realizations  $\{\overline{\Psi}^{(k)}\}_{k=1}^\mu$ 
           Tolerance parameter  $\epsilon_{KL}$ 
  Compute  $\mu_{\overline{\Psi}} \simeq \frac{1}{\mu} \sum_{k=1}^\mu \overline{\Psi}^{(k)}$ 
  Compute  $[\mathbf{C}_{\overline{\Psi}}] \simeq \frac{1}{(\mu-1)} \sum_{k=1}^\mu \tilde{\psi}^{(k)} \tilde{\psi}^{(k)T}$  and solve the eigenvalues
  problem
  Select  $M$  such that  $\sqrt{1 - \frac{\sum_{j=1}^M \lambda_j}{\text{tr}[\mathbf{C}_{\overline{\Psi}}]}} = \epsilon_{KL}^M < \epsilon_{KL}$ 
  Compute  $\{\zeta^{(k)}\}_{k=1}^\mu$  with  $\zeta_j^{(k)} = \frac{1}{\sqrt{\lambda_j}} \varphi_j^T(\overline{\Psi}^{(k)} - \mu_{\overline{\Psi}})$ 
  output: Set of realizations  $\{\zeta^{(k)}\}_{k=1}^\mu$ 
end

Identification on polynomial chaos basis;
begin
  input : Set of realizations  $\{\zeta^{(k)}\}_{k=1}^\mu$ 
           Parameters  $N_g, N_d$ 
  for  $j = 1$  to  $M$  do
    | Determine  $M_j^{mode}$ 
    | for  $\ell = 1$  to  $M_j^{mode}$  do
    | | Solve recurrent optimization problem  $\mathcal{P}_\ell$ 
    | end
    | output: Decomposition of  $\zeta_j$  under the form
           
$$\zeta_j(\widehat{\Xi}_j, \Xi) \simeq \sum_{i=1}^{M_j^{mode}} \mathbb{I}_{K_{j,i}}(\widehat{\Xi}_j) \left( \sum_{\alpha=1}^N y_{j,i}^\alpha H_\alpha(\Xi) \right)$$

  end
  output: PC coefficients  $\{\mathbf{y}^\alpha, \alpha = 1, \dots, N\}$ 
end

```

**Algorithm 1:** Pseudo-algorithm of the proposed methodology.

In numerical example 6.1, we only use the polynomial chaos representation defined by Eq. (24), associated with the identification technique proposed in [39], since the components of random vector  $\bar{\Psi}$  are random variables with uni-modal probability density functions. This method is denoted by strategy (UM). However, in numerical example 6.2, since the components of the random vector  $\bar{\Psi}$  are characterized by multi-modal probability density functions, we also use the representation (28) based on mixture of polynomial chaos proposed in Sec. 4.2. This technique is denoted strategy (MM). In this example, and in the mesoscopic application 6.3, the performances of the two strategies (UM) and (MM) are compared.

## 6. Applications

In this section, we detail three numerical examples to demonstrate the efficiency of the proposed approach. Numerical examples 6.1 and 6.2 aim at identifying the apparent (or effective) mechanical properties for two different sets of parameters for the probabilistic model of the geometry of the microstructure. In example 6.1, the components of random vector  $\bar{\Psi}$  are uni-modal (*i.e.* the probability density function only possesses one local maximum) while in example 6.2, the components of random vector  $\bar{\Psi}$  are multi-modal (*i.e.* the probability density functions possesses several local maxima). Numerical example 6.3 consists in a mesoscale structural problem for which the apparent mechanical properties are computed with the microscale problem studied in Sec. 6.2. For each application, the proposed approach is compared with reference solutions computed with classical methods in order to show its efficiency.

### 6.1. Application 1: microstructural problem (A)

#### 6.1.1. Problem definition

At the microscopic level, we consider a hyperelastic heterogeneous material characterized by a compressible Neo-hookean model given by the potential defined in Eq. (5). For the matrix, the Young modulus is  $E^m = 10^9$  Pa and the Poisson ratio is  $\nu^m = 0.4$ . For the inclusions,  $E^f = 10^{11}$  MPa and  $\nu^f = 0.3$ . One should notice the large contrast between the two phases which is not an issue with the NEXP method. The large scale strain domain  $\Delta_{\bar{\mathcal{C}}}$  is chosen such as  $\Delta_{\bar{\mathcal{C}}} = \Delta_{\bar{\mathcal{C}}_1} \times \Delta_{\bar{\mathcal{C}}_2} \times \Delta_{\bar{\mathcal{C}}_6} = [0.9, 1.5] \times [0.9, 1.5] \times [-0.1, 0.5]$  and we use  $p = 7$  points along each axis  $\bar{\mathcal{C}}_i$ . The random vector  $\bar{\Psi}$  to determined

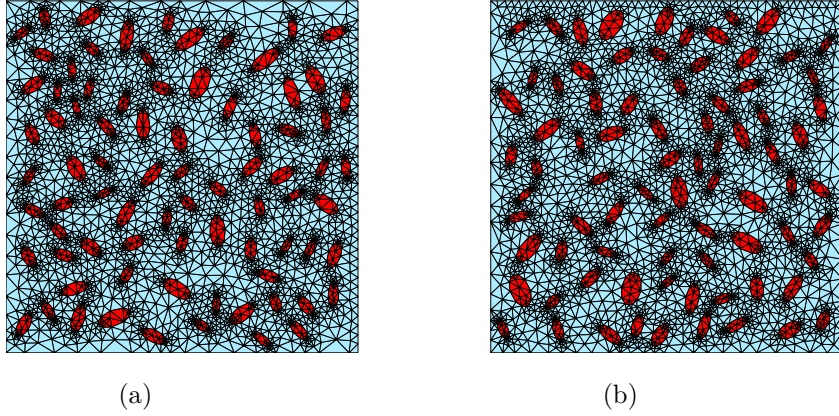


Figure 3: Finite element meshes of two realizations of the geometry of the microstructure.

is thus made of 343 components. The input parameters for the random generator are the following ones: number of random variables  $m = 6,000$ , spatial correlation parameter  $\rho = 10^{-5}$ , number of realizations  $\mu = 350$ , coefficient of variation  $\delta = 0.5$  and number of fibers  $N_f = 80$ . Fig. 3 illustrates two finite element meshes corresponding to two realizations of the microstructure.

#### 6.1.2. Analysis of the reduced-order model

In this section, we propose to analyze the efficiency of the expansion (21). Fig. 4 displays the graph of error function  $\epsilon_{KL}^M$  defined by (22) according to the number of modes  $M$ . A very fast convergence of the error can be observed. Indeed, with only  $M = 5$  modes, an error inferior to  $10^{-3}$  is reached. Fig. 5 displays the probability density function of  $\bar{\Psi}$  for  $\bar{C}_{11} = 1.5$ ,  $\bar{C}_{22} = 1.5$  and  $\bar{C}_{12} = 0.5$  and the probability density functions of each retained reduced-order random variable  $\zeta_j$ . It can be observed that the probability density functions of components of random vector  $\bar{\Psi}$  are uni-modal. The same remark can be made for each reduced-order random variable  $\zeta_j$ . In the following sections, we focus on the identification of the reduced-order random variables  $\{\zeta_j, j = 1, \dots, 5\}$  on polynomial chaos expansions with strategy (UM) only since the various reduced-order random variables  $\zeta_j$  are not characterized by probability density functions which possess several modes. Convergence analysis with respect to the length  $N_g$  of the germ  $\Xi$  and the maximum degree  $N_d$  of the polynomial chaos are carried out.

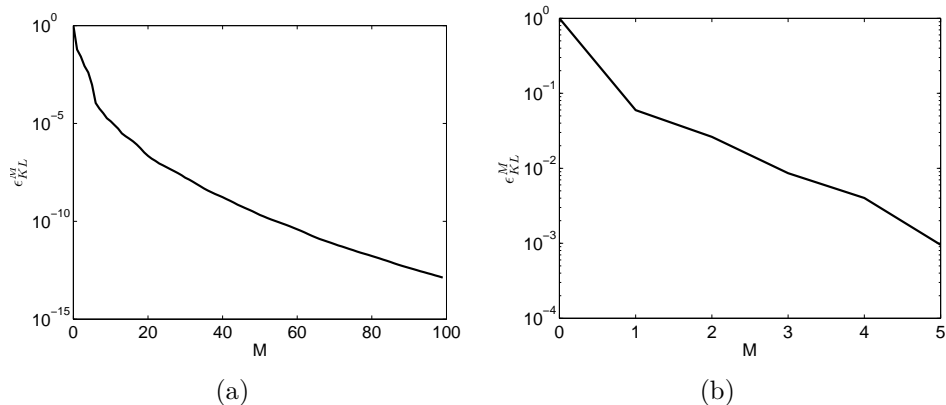


Figure 4: Graphs of the error function  $M \mapsto \epsilon_{KL}^M$  for  $M = 1, \dots, 100$  (a) and for  $M = 1, \dots, 5$  (b).

### 6.1.3. Identification of the reduced-order model

In this section, the calculation of the vector-valued coefficients  $\mathbf{y}^1, \dots, \mathbf{y}^N$  in  $\mathbb{R}^M$  of the polynomial chaos expansion (24) is performed using the random search algorithm introduced in [39]. A convergence analysis is carried out using the  $L^1$ -log error function defined by Eqs. (29) and (30) with respect to the length of germ  $N_g = 1, \dots, 4$  and maximum degree  $N_d = 8, \dots, 22$  of the polynomial chaos. Each recurrent optimization problem  $\mathcal{P}_l$  for  $l = 1, \dots, 5$  is solved using  $\mu_{rs} = 5,000$  independent realizations. The total number of independent realizations performed with the algorithm is then  $2 \times \sum_{j=1}^5 \mu_{rs} = 50,000$ . The number  $\mu_{PC}$  of independent realizations of  $\Xi$  used to estimate the probability density functions of  $\zeta_j^{PC}$  is  $\mu_{PC} = 15,000$ . In terms of computational costs, the CPU times are respectively 9 and 93 minutes for configurations  $N_g = 1$  and  $N_d = 8$ , and configuration  $N_g = 4$  and  $N_d = 22$ , using a computer with 8 cores. Fig. 6 (a) displays the graph of the  $L^1$ -log error function  $N_d \mapsto err(N_g, N_d)$  for  $N_g = 1, \dots, 4$ . We can observe a bad rate of convergence of the error indicator for lengths of germ  $N_g = 1$  and  $N_g = 2$  and a slow convergence for length of germ  $N_g = 3$ . Increasing the number  $\mu_{rs}$  of independent realizations could slightly improve the results in terms of the error level, but would significantly increase the CPU times. On the other hand, we can notice a good convergence for length of germ  $N_g = 4$  for which a reasonable convergence is reached for maximum degree of polynomial chaos  $N_d = 18$ . Moreover, on Fig. 6 are also displayed the comparison of the probability density functions in log-

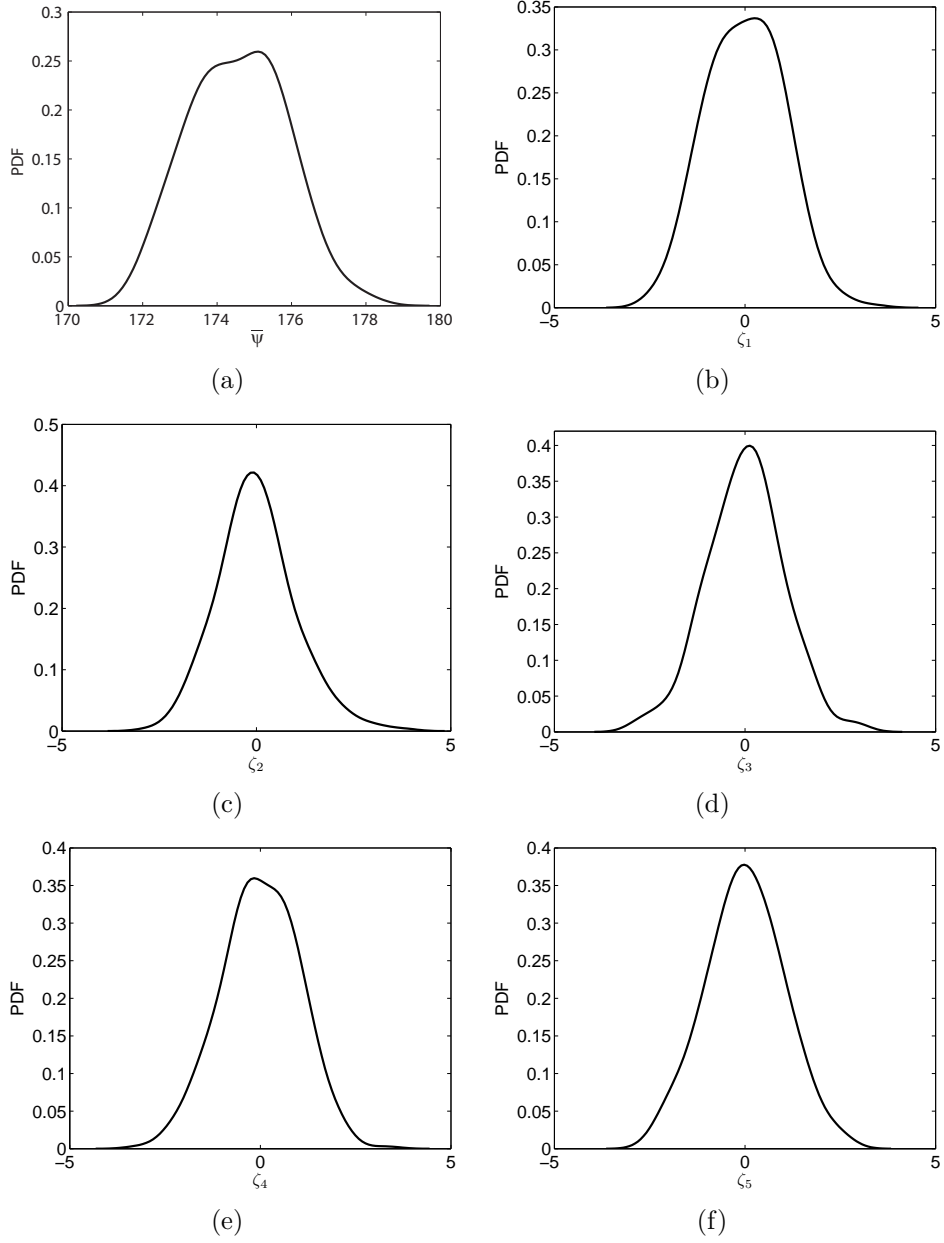


Figure 5: (a): PDF of  $\overline{\Psi}(\overline{\mathbf{C}})$  for  $\overline{C}_{11} = 1.5$ ,  $\overline{C}_{22} = 1.5$  and  $\overline{C}_{12} = 0.5$ ; (b) to (f): PDFs of each reduced-order random variable  $\zeta_j$  for  $j = 1, \dots, 5$ .

scale of random variables  $\zeta_j$  obtained with the  $\mu$  realizations of the reduced-order model (*e.g.* reference solution) and estimated with the polynomial chaos expansions corresponding to  $N_g = 1, \dots, 4$  and for  $N_d$  leading to the lowest value of the  $L^1$ -log error function. We have thus retained the following solutions:  $N_g = 1$  with  $N_d = 20$ ,  $N_g = 2$  with  $N_d = 8$ ,  $N_g = 3$  with  $N_d = 20$  and  $N_g = 4$  with  $N_d = 18$ . We can clearly observe that the solution corresponding to  $N_g = 4$  with  $N_d = 18$  leads to a very good identification of all the reduced-order random variables  $\zeta_j$  while the other approximated solutions, *i.e.* for  $N_g = 1, \dots, 3$ , lead to poor results regarding the reference solution.

#### 6.1.4. Quality assessment of the apparent constitutive law

We now focus on the analysis of the apparent mechanical quantities  $\overline{\Psi}$ ,  $\overline{\mathbf{S}}$  and  $\overline{\mathbf{L}}$  characterizing the apparent constitutive equations. We propose to use the best solutions for each length of germ  $N_g$  according to the  $L^1$ -log error function also used for Fig. 6. The computation of quantities  $\overline{S}_{11}$  and  $\overline{L}_{1111}$  is done using the approximation of the apparent quantities  $\overline{\Psi}$ ,  $\overline{\mathbf{S}}$  and  $\overline{\mathbf{L}}$  through Eqs. (13) and (14) to (16). This step requires to compute the separated variables representation for each realizations generated by the polynomial chaos expansions. Fig. 7 illustrates the probability density functions for quantities  $\overline{\Psi}$ ,  $\overline{S}_{11}$  and  $\overline{L}_{1111}$  for the two following large scale strain states: (i)  $\overline{C}_{11} = 1.5$ ,  $\overline{C}_{22} = 1.5$  and  $\overline{C}_{12} = 0.5$ , (ii)  $\overline{C}_{11} = 1.35$ ,  $\overline{C}_{22} = 0.95$  and  $\overline{C}_{12} = 0.15$ . The reference solutions correspond to independent nonlinear FEM computations according to apparent strain states (i) and (ii) for geometries of the microstructure generated from the set of geometrical parameters  $\{\boldsymbol{\xi}^{(k)}\}_{k=1}^{\mu}$ . We can observe that solutions corresponding to  $N_g = 1$  up to  $N_g = 3$  lead to bad approximations of the apparent quantities while solution corresponding to  $N_g = 4$  leads to a very good approximation with respect to the reference solution. Finally we can notice that the statistic fluctuations are very low: indeed, the coefficient of variation of  $\overline{S}_{11}$  is equal to 0.57% for the solution corresponding to  $N_g = 4$  and to 0.58% for the reference solution. The apparent mechanical properties can thus be considered as deterministic and this model at the small scale can be used in a structural problem where the two scales are the microscale and the macroscale.

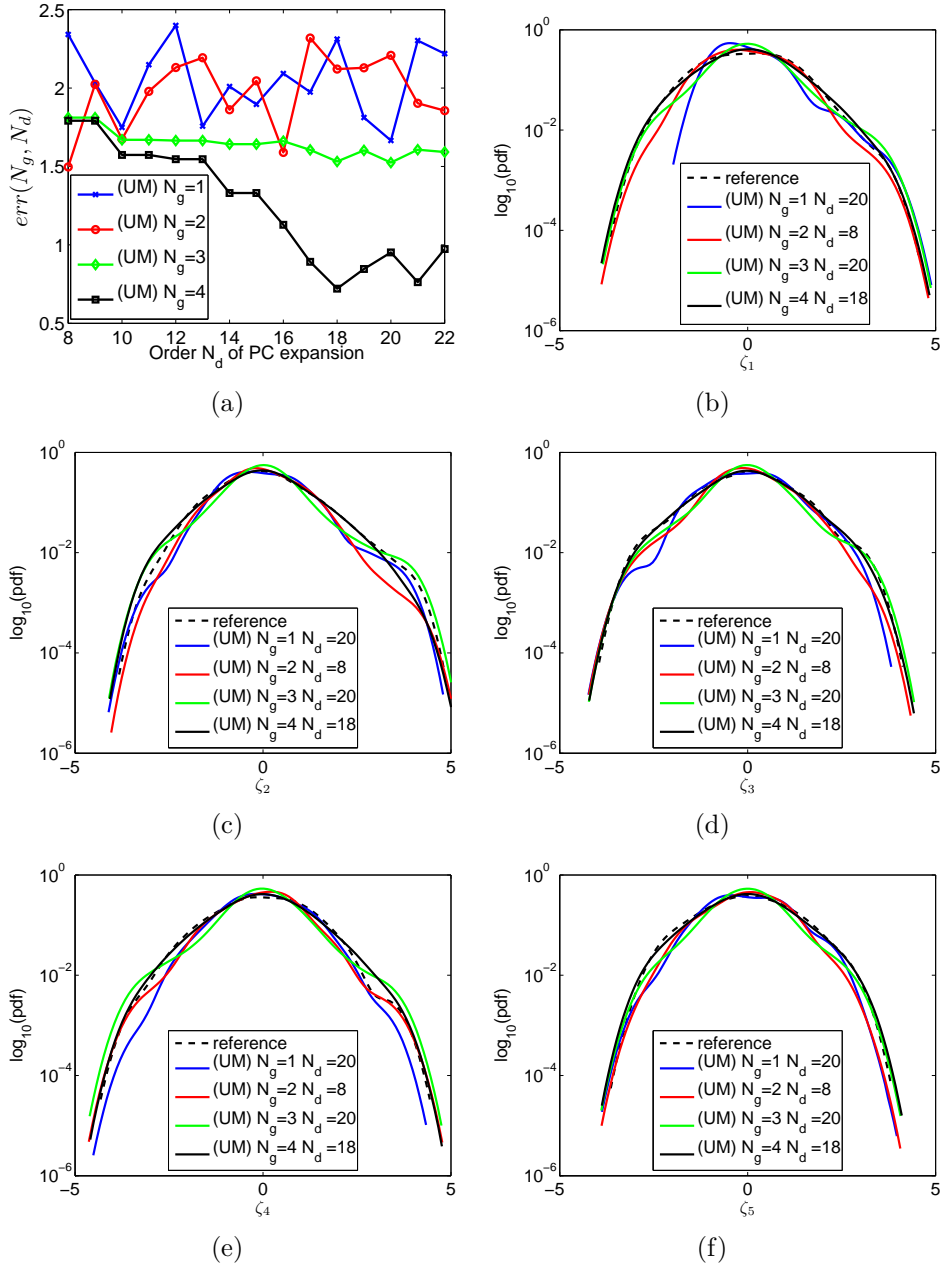


Figure 6: (a): Graph of function  $N_d \mapsto err(N_g, N_d)$  for  $N_g = 1, \dots, 4$  and  $N_d = 8, \dots, 22$ ; (b) to (f): PDFs of  $\zeta_j$ ,  $j = 1, \dots, 5$  respectively computed with the reference solution and the identification strategy (UM).

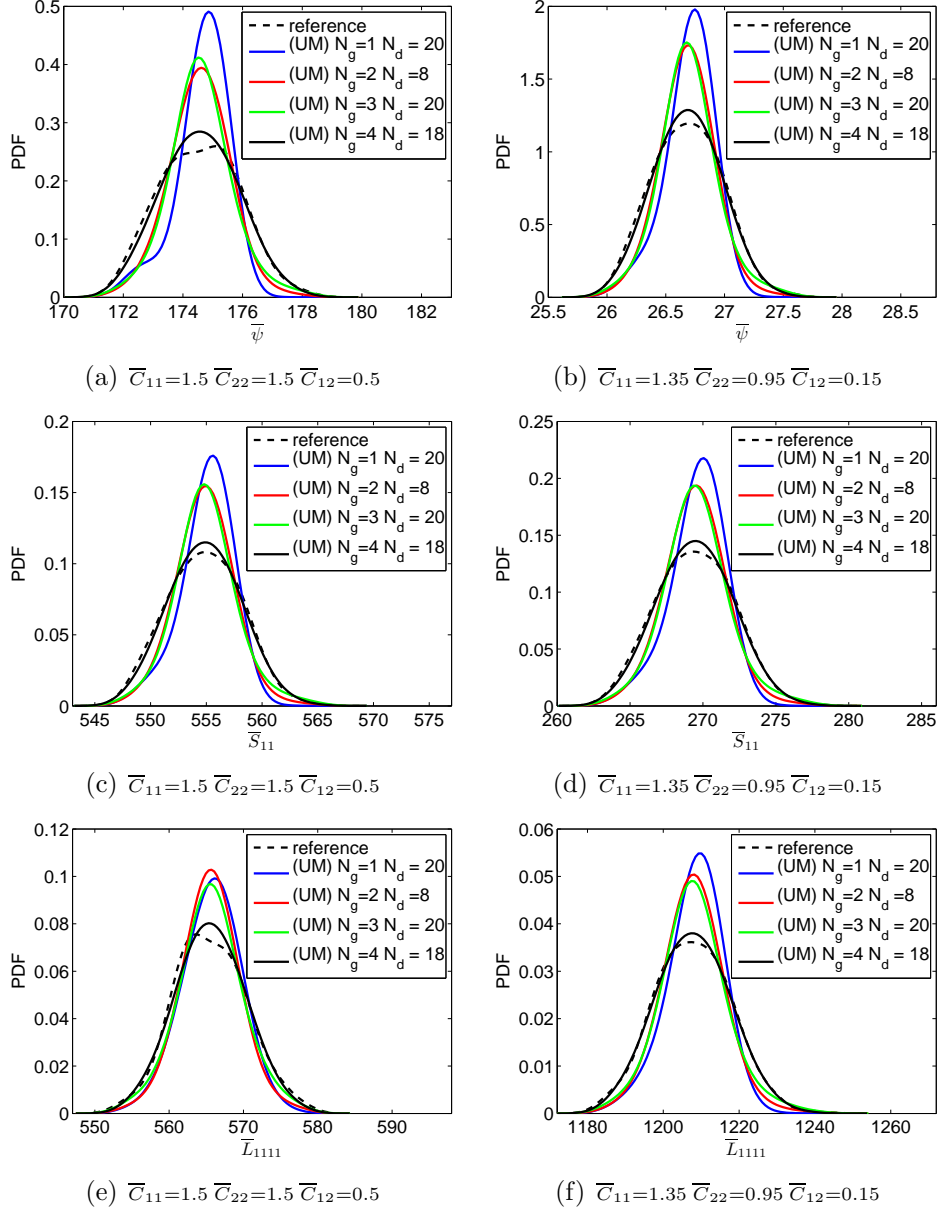


Figure 7: (a), (c) and (e): PDFs of  $\bar{\Psi}(\bar{\mathbf{C}})$ ,  $\bar{S}_{11}(\bar{\mathbf{C}})$  and  $\bar{L}_{1111}(\bar{\mathbf{C}})$  computed with strategy (UM) for large scale strain states (i); (b), (d) and (f): PDFs of  $\bar{\Psi}(\bar{\mathbf{C}})$ ,  $\bar{S}_{11}(\bar{\mathbf{C}})$  and  $\bar{L}_{1111}(\bar{\mathbf{C}})$  computed with strategy (UM) for large scale strain states (ii) .

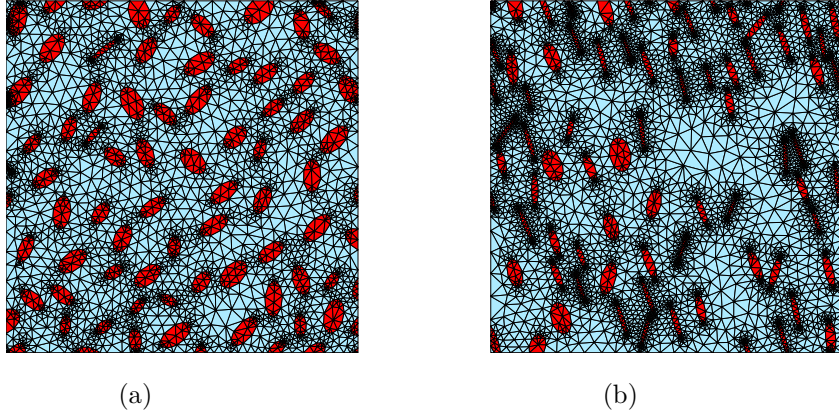


Figure 8: Finite element meshes of two realizations of the geometry of the microstructure.

## 6.2. Application 2: small scale problem (B)

### 6.2.1. Problem definition

The aim of this example is also to demonstrate the efficiency of the proposed method and the accuracy of the resulting solution through comparisons with standard approaches. The parameters of the hyperelastic heterogeneous material are the same as the ones used in example 6.1. The input parameters for the random generator are also the same except for the spatial correlation parameter  $\rho$  which is taken equal to 0.5. This choice involves significant changes in the random geometry of the microstructure (volume fraction and shape of the fibers) as it can be seen in Fig. 8 which displays two finite element meshes corresponding to two realizations of the microstructure.

### 6.2.2. Analysis of the reduced-order model

In this section, we propose to analyze the efficiency of the expansion (21). Fig. 9 displays the graph of error function  $\epsilon_{KL}^M$  defined by (22) according to the number of modes  $M$ . As in numerical example 6.1, we can observe a very fast convergence of the error (error inferior to  $10^{-3}$  with  $M = 5$ ). Fig. 10 displays the probability density function of  $\bar{\Psi}$  for  $\bar{C}_{11} = 1.5$ ,  $\bar{C}_{22} = 1.5$  and  $\bar{C}_{12} = 0.5$  and the probability density functions of each retained reduced-order random variable  $\zeta_j$ . We can clearly observe that the strain energy density function is multi-modal, which is the case for all large scale strain states. This multi-modal nature is mainly due to the variability of the aspect ratio involving variations in the volume fraction as it can be seen in Fig. 8.

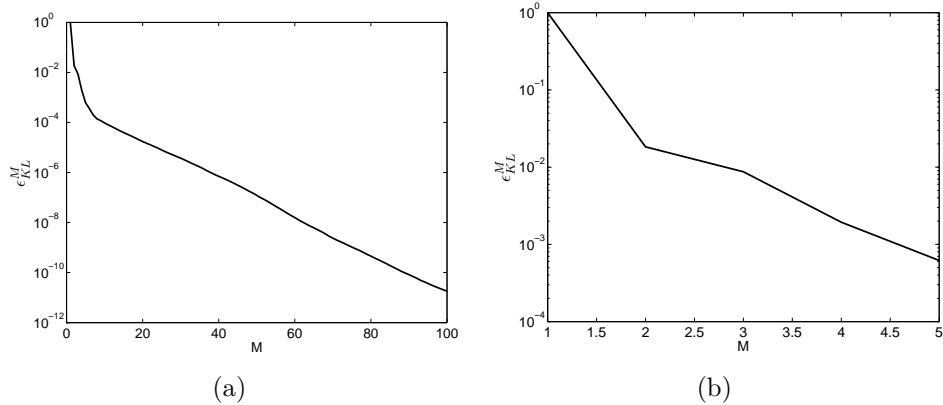


Figure 9: Graphs of the error function  $M \mapsto \epsilon_{KL}^M$  for  $M = 1, \dots, 100$  (a) and for  $M = 1, \dots, 5$  (b).

Thus, random variable  $\zeta_1$ , which is the most important in the reduced-order model, presents also the same kind of modes. We can also notice that the probability density function of random variable  $\zeta_3$  possesses several modes which may be important to capture. In the following sections, we focus on the identification of the reduced-order random variables  $\zeta_j$  for  $j = 1, \dots, 5$  on polynomial chaos expansions with the two proposed strategies (UM) and (MM). Convergence analysis with respect to the length  $N_g$  of the germ  $\Xi$  and the maximum degree  $N_d$  of the polynomial chaos are performed.

### 6.2.3. Identification procedure with strategy (UM)

In this section, the calculation of the vector-valued coefficients  $\mathbf{y}^1, \dots, \mathbf{y}^N$  in  $\mathbb{R}^M$  of the polynomial chaos expansion defined by Eq. (24) is performed using the random search algorithm introduced in [39]. The multi-modal nature of random variables  $\zeta_j$  is not specifically taken into account. A convergence analysis is carried out using the  $L^1$ -log error function defined by Eqs. (29) and (30) with respect to the length of germ  $N_g = 1, \dots, 4$  and maximum degree  $N_d = 8, \dots, 22$  of the polynomial chaos. Each recurrent optimization problem  $\mathcal{P}_l$  for  $l = 1, \dots, 5$  is solved using  $\mu_{rs} = 5,000$  independent realizations. The total number of independent realizations performed with the algorithm is then  $2 \times \sum_{j=1}^5 \mu_{rs} = 50,000$ . The number  $\mu_{PC}$  of independent realizations of  $\Xi$  used to estimate the probability density functions of  $\zeta_j^{PC}$  is  $\mu_{PC} = 15,000$ . Fig. 11 (a) displays the graphs of  $L^1$ -log error function  $N_d \mapsto err(N_g, N_d)$  for  $N_g = 1, \dots, 4$ . We can observe a bad rate of conver-

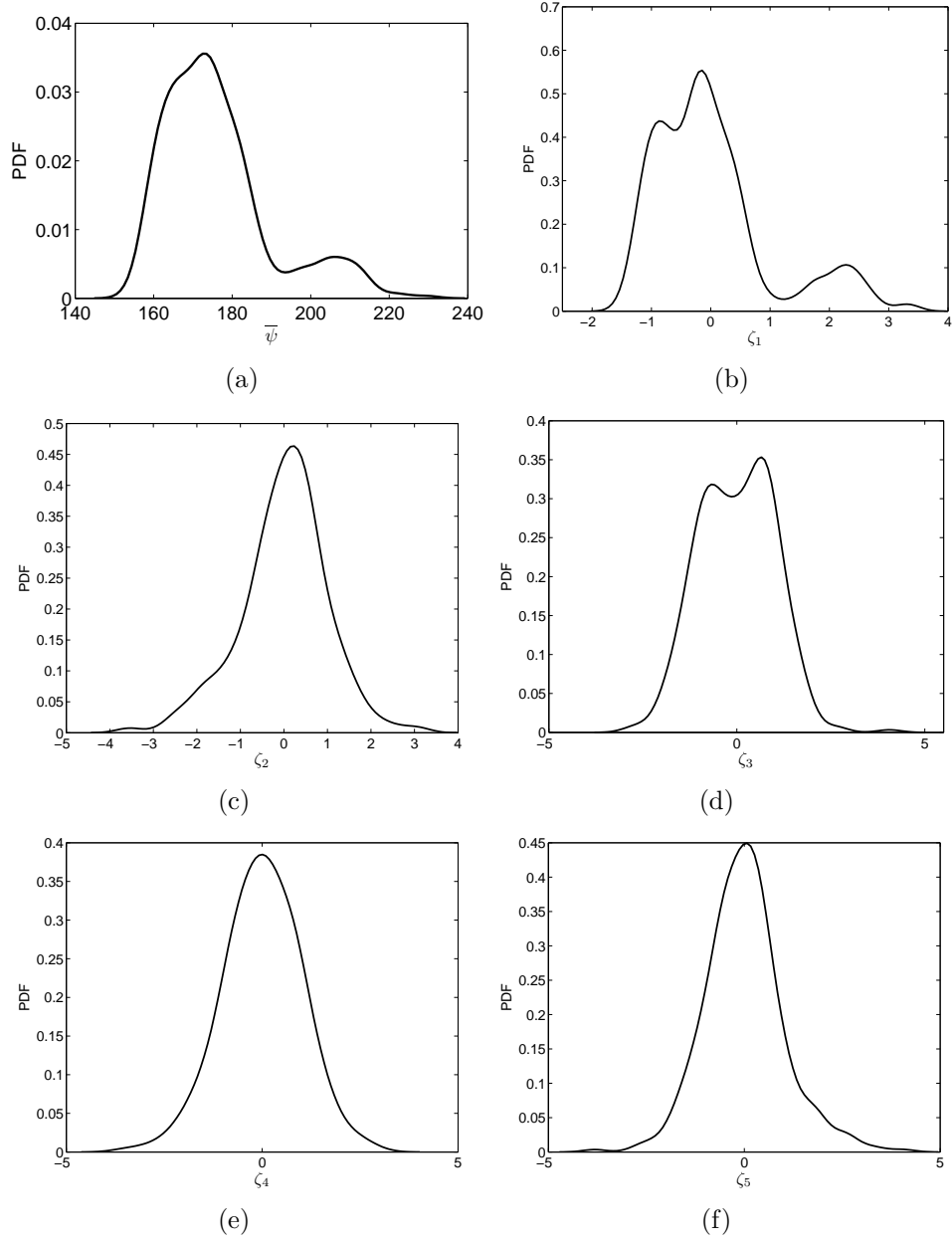


Figure 10: (a): PDFs of  $\bar{\Psi}(\bar{C})$  for  $\bar{C}_{11} = 1.5$ ,  $\bar{C}_{22} = 1.5$  and  $\bar{C}_{12} = 0.5$ ; (b) to (f): PDFs of each reduced-order random variable  $\zeta_j$  for  $j = 1, \dots, 5$ .

gence of the error indicator for lengths of germ  $N_g = 1$  and  $N_g = 2$  and slow convergences are observed for  $N_g = 3$  and  $N_g = 4$ . Moreover, in Fig. 11 are also displayed the comparison of the probability density functions in log-scale of random variables  $\zeta_j$  obtained with the  $\mu$  realizations of the reduced-order model (*e.g.* reference solution) and estimated with the polynomial chaos expansions corresponding to  $N_g = 1, \dots, 4$  and for  $N_d$  leading to the lowest value of the  $L^1$ -log error function. We can indeed notice bad results for all the displayed solutions and more particularly for the reduced-order random variables  $\zeta_1$  and  $\zeta_3$  which present several modes. Regarding the results given in Fig. 11, we propose to analyze two ways for improving the results: increasing the maximum order  $N_d$  of the polynomial chaos expansions for a fixed length of germ  $N_g = 1$ , and increasing the length of germ  $N_g$  for a fixed maximum order  $N_d = 10$ . Fig. 12 displays the graphs of error function  $N_d \mapsto err(N_g, N_d)$  for a fixed length of the germ,  $N_g = 1$ , and maximum order,  $N_d = 25, \dots, 60$ , and of error  $N_g \mapsto err(N_g, N_d)$  for  $N_g = 1, \dots, 7$  and a fixed maximum order  $N_d = 10$ . Both strategies allows decreasing the level of error, however, we can notice that increasing the length  $N_g$  of the germ leads us to better results, with a convergence reached for  $N_g = 5$ , and an inferior level of error regarding the results for  $N_g = 1$  and  $N_d = 35$  for which the convergence seems to be reached. Nevertheless, Fig. 12 also illustrates the graphs of error  $N_d \mapsto err_1(N_g, N_d)$  and  $N_g \mapsto err_1(N_g, N_d)$  corresponding to the reduced-order random variable  $\zeta_1$ , for which the probability density function possesses several modes. We can observe that increasing the maximum order,  $N_d$ , allows a better representation of random variable  $\zeta_1$  to be obtained while increasing the length  $N_g$  of the germ does not. It can thus be concluded that the best way to represent the reduced-order random vector  $\zeta$  on a polynomial chaos basis would consists in using high values of both  $N_g$  and  $N_d$ . However, such a basis would involve a very high number of coefficients in the polynomial chaos expansions and would lead to too large computational times. It is thus proposed to use the strategy (MM) based on mixture of polynomial chaos detailed in Sec. 4.2 in order to improve the convergence of the identification procedure with similar computational times. The results are given in the following subsection.

#### 6.2.4. Identification procedure with strategy (MM)

In this section, we show the results obtained with the strategy based on the prior stochastic model relying on the mixture of probability laws model described in Section 4.2 and for which the calculation of the vector-valued

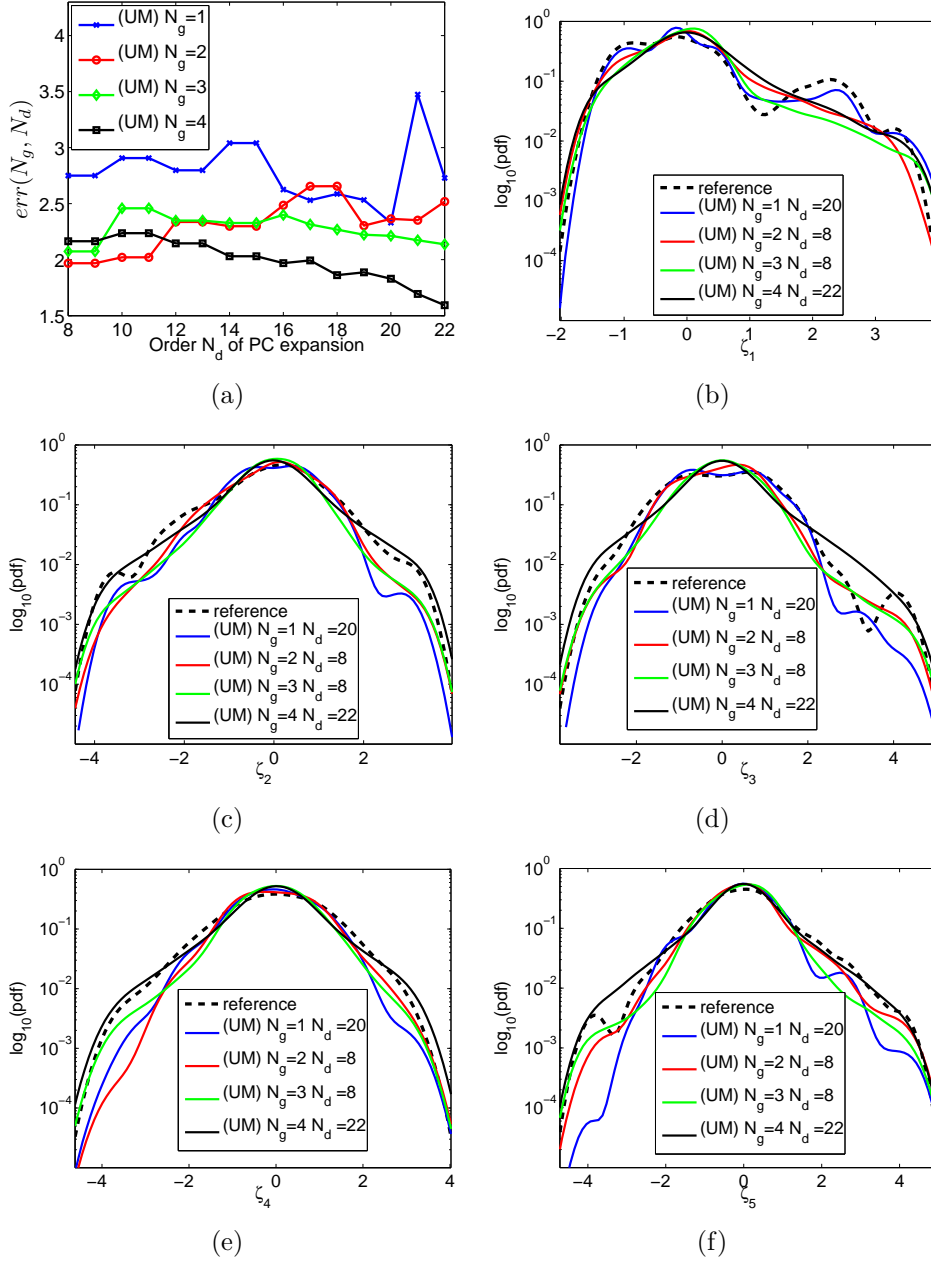


Figure 11: (a): Graph of function  $N_d \mapsto err(N_g, N_d)$  for  $N_g = 1, \dots, 4$  and  $N_d = 8, \dots, 22$  for strategy (UM); (b) to (f): PDFs of  $\zeta_j$ ,  $j = 1, \dots, 5$  computed with the reference solution and strategy (UM).

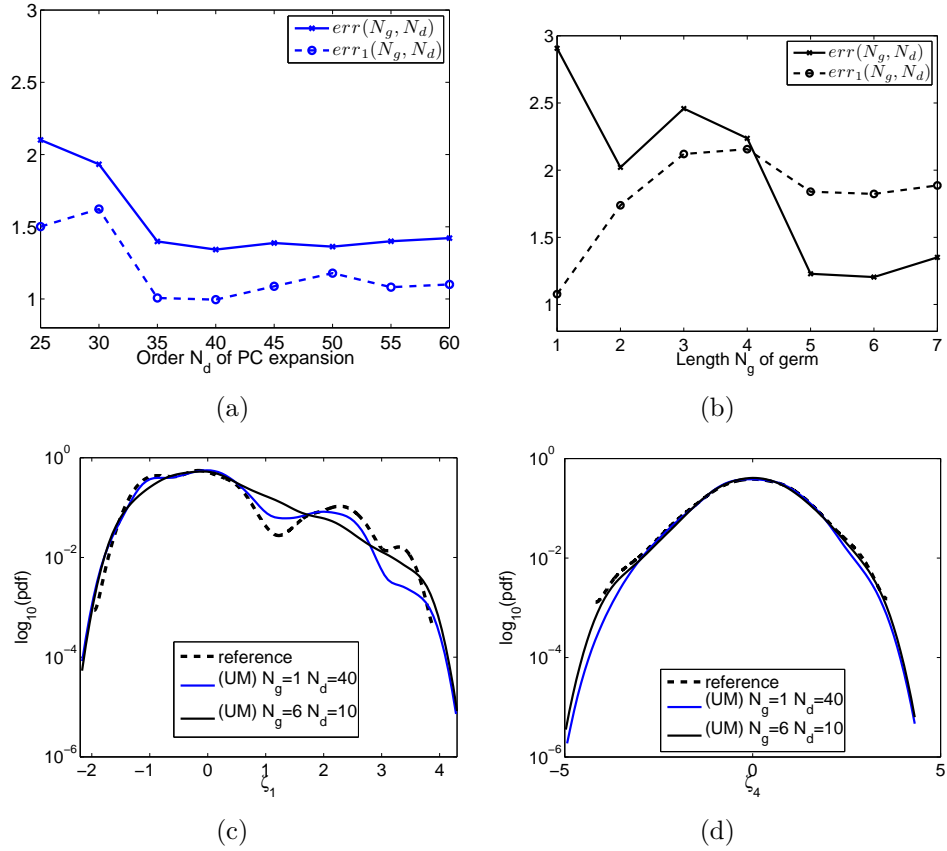


Figure 12: (a): Graphs of functions  $N_d \mapsto err(N_g, N_d)$  and  $N_d \mapsto err_1(N_g, N_d)$  for  $N_g = 1$  and  $N_d = 1, \dots, 60$ ; (b): Graphs of functions  $N_g \mapsto err(N_g, N_d)$  and  $N_d \mapsto err_1(N_g, N_d)$  for  $N_g = 1, \dots, 7$  and  $N_d = 10$ ; (c) and (d) PDFs of  $\zeta_1$  and  $\zeta_4$  computed with the identification strategy (UM) and the reference solution.

coefficients of the polynomial chaos expansion defined by Eq. (28) is also performed using the random search algorithm detailed in [39]. The aim is to accelerate the identification which means obtaining better results without increasing the number of coefficients in the polynomial chaos expansions. The multi-modal nature of the probability density function of random variables  $\zeta_j$  is thus taken into account. The number of modes  $M_j^{mode}$  (*i.e.* number of local maxima) for each  $\zeta_j$  are:  $M_1^{mode} = 5$ ,  $M_2^{mode} = 2$ ,  $M_3^{mode} = 6$ ,  $M_4^{mode} = 3$  and  $M_5^{mode} = 7$ . One should note that all detected modes have been taken into account, even the smallest ones which can appear as spurious modes and are not visible in Fig. 10. However, this greatly allows improving the identification procedure. As in the previous section, a convergence analysis is carried out using the  $L^1$ -log error function defined by Eqs. (29) and (30) with respect to the length of germ  $N_g = 2, \dots, 4$  and maximum degree  $N_d = 8, \dots, 22$  of the polynomial chaos. All recurrent optimization problems are solved using  $\mu_{rs} = 1,000$  independent realizations. Since, the mixture of probability laws is here used, the number of recurrent optimization problems  $\mathcal{P}_l$  is increased to the value corresponding to the total number of modes  $M^{mode} = 23$ . The total number of independent realizations performed with the algorithm is then  $2 \times \sum_{j=1}^{23} \mu_{rs} = 46,000$ . The number  $\mu_{PC}$  of independent realizations of  $\Xi$  used to estimate the probability density functions is  $\mu_{PC} = 15,000$ .

Fig. 13 (a) displays the graphs of  $L^1$ -log error function  $N_d \mapsto err(N_g, N_d)$  for  $N_g = 2, \dots, 4$  and  $N_d = 8, \dots, 22$ . For  $N_g = 2$ , a bad rate of convergence of the error indicator is observed. However, the values of the  $L^1$ -log error function are lower than the ones obtained with the strategy (UM). A slow convergence is observed for  $N_g = 3$  and a good rate of convergence of the  $L^1$ -log error function is clearly seen for  $N_g = 4$  for which a reasonable solution seems to be reached for  $N_d = 17$ . Fig. 13 also displays the comparison of the probability density functions in log-scale of random variables  $\zeta_j$  obtained with the  $\mu$  realizations of the reduced-order model, and estimated with the polynomial chaos expansions corresponding to  $N_g = 2, \dots, 4$  and for  $N_d$  leading to the lowest value of the  $L^1$ -log error function. We can clearly notice better results than those obtained with the strategy (UM). For instance, concerning random variable  $\zeta_1$ , we can see that the different modes are well represented especially for the solution corresponding to  $N_g = 4$  and leading to the smallest value of the  $L^1$ -log error function. In terms of computational costs, the PCU times are respectively 6 and 65 minutes for configuration  $N_g = 1$  and  $N_d = 8$ , and configuration  $N_g = 4$  and  $N_d = 22$ , using a computer

cluster with 8 cores. One should note that the CPU times are lower than the ones obtained with strategy (UM) mainly because the number of independent realizations corresponds here to  $\mu_{rs} = 1000$ .

#### 6.2.5. Quality assessment of the apparent constitutive law

After the study of the identification of the reduced-order model on the polynomial chaos expansions, we propose to analyze the results on the apparent mechanical quantities  $\bar{\Psi}$ ,  $\bar{\mathbf{S}}$  and  $\bar{\mathbf{L}}$  characterizing the apparent constitutive equations. We propose to use the best solutions of the two identification strategies according to the  $L^1$ -log error function. Thus, we have retained the two following solutions: strategy (UM) with  $N_g = 4$  and  $N_d = 22$  and strategy (MM) with  $N_g = 4$  and  $N_d = 18$ . We first focus on the apparent strain energy density function. Fig. 14 illustrates the probability density functions of  $\bar{\Psi}(\bar{\mathbf{C}})$  for the following large scale strain states: (i)  $\bar{C}_{11} = 0.9$ ,  $\bar{C}_{22} = 0.9$  and  $\bar{C}_{12} = -0.1$ , (ii)  $\bar{C}_{11} = 1.1$ ,  $\bar{C}_{22} = 1.3$  and  $\bar{C}_{12} = 0.3$ , (iii)  $\bar{C}_{11} = 1.4$ ,  $\bar{C}_{22} = 1.2$  and  $\bar{C}_{12} = 0.2$ , and (iv)  $\bar{C}_{11} = 1.5$ ,  $\bar{C}_{22} = 1.5$  and  $\bar{C}_{12} = 0.5$ . On this figure, the different PDFs have been plotted with a linear scale since the authors want to point out the capacity of the different identification strategies to capture the multi-modal nature of the apparent strain energy density function. We can thus clearly observe that the strategy (UM) is unable to capture the different modes of the various PDFs whereas strategy (MM) leads to very good solutions according to the reference solution. Indeed, this approach leads to the better results for the approximation of  $\bar{\Psi}$ . We then focus on the post-processing of the identified solutions and its quality. We thus focus on three quantities,  $\bar{\Psi}(\bar{\mathbf{C}})$ ,  $\bar{S}_{11}(\bar{\mathbf{C}})$  and  $\bar{L}_{1111}(\bar{\mathbf{C}})$  for particular values of tensor  $\bar{\mathbf{C}}$  which do not belong to the initial set of realizations  $\{\bar{\Psi}^{(k)}\}_{k=1}^{\mu}$  used in the principal component analysis. Thus, we use, as post-processing, the separated variables representation leading to the approximation of the apparent quantities  $\bar{\Psi}$ ,  $\bar{\mathbf{S}}$  and  $\bar{\mathbf{L}}$  through Eqs. (13) and (14) to (16). This step requires to compute the separated variables representation for each realizations generated by the polynomial chaos expansions computed with the two strategies (UM) and (MM). We have chosen four different cases of large scale strain states: (v)  $\bar{C}_{11} = 0.95$ ,  $\bar{C}_{22} = 0.95$  and  $\bar{C}_{12} = -0.05$ , (vi)  $\bar{C}_{11} = 1.22$ ,  $\bar{C}_{22} = 1.22$  and  $\bar{C}_{12} = 0.22$ , (vii)  $\bar{C}_{11} = 1.47$ ,  $\bar{C}_{22} = 1.33$  and  $\bar{C}_{12} = 0.43$ , and (viii)  $\bar{C}_{11} = 1.18$ ,  $\bar{C}_{22} = 1.12$  and  $\bar{C}_{12} = 0.42$ . The reference solutions correspond to independent nonlinear FEM computations according to apparent strain states (v) to (viii) for geometries of the microstructure generated from the set of geometrical parameters  $\{\boldsymbol{\xi}^{(k)}\}_{k=1}^{\mu}$ . Figs. 15, 16

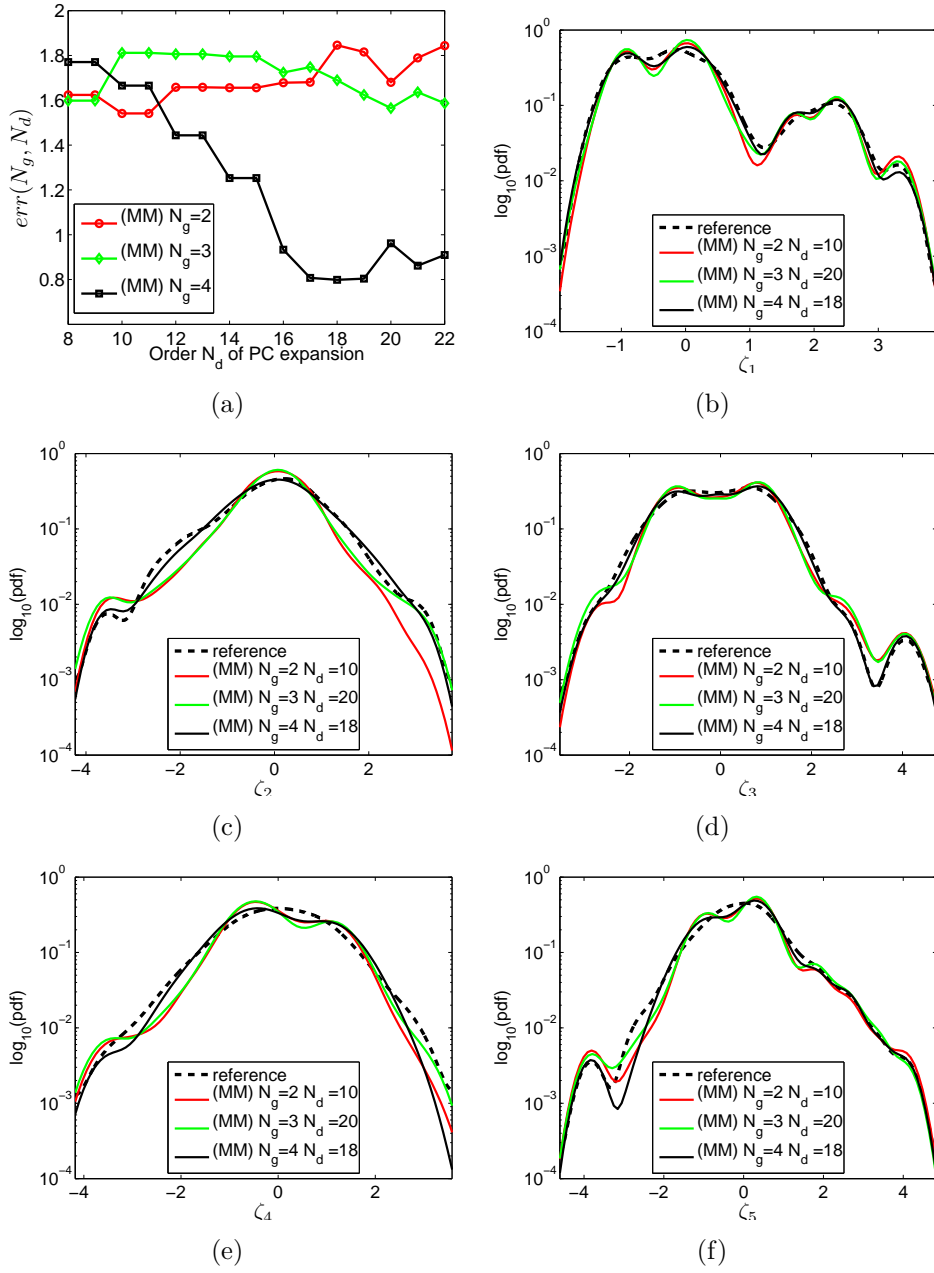


Figure 13: (a): Graph of function  $N_d \mapsto err(N_g, N_d)$  for  $N_g = 2, \dots, 4$  and  $N_d = 8, \dots, 22$  for strategy (MM); (b) to (f): PDFs of  $\zeta_j$ ,  $j = 1, \dots, 5$  computed with the reference solution and strategy (MM).

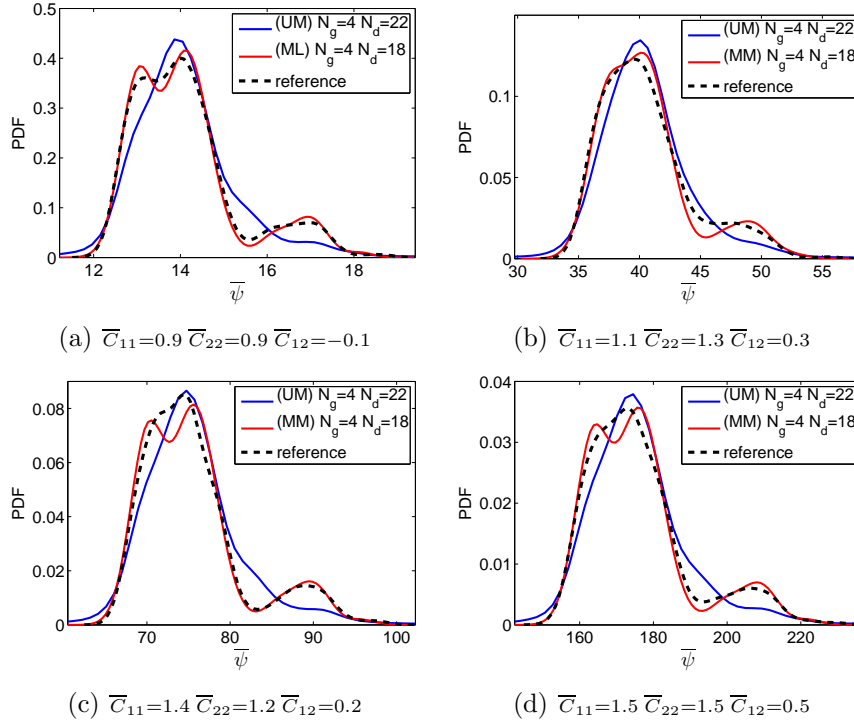


Figure 14: PDFs of  $\bar{\Psi}(\bar{\mathbf{C}})$  computed with strategies (UM), (MM) and the reference solution; (a) large scale strain state (i); (b) large scale strain state (ii); (c) large scale strain state (iii); (d) large scale strain state (iv).

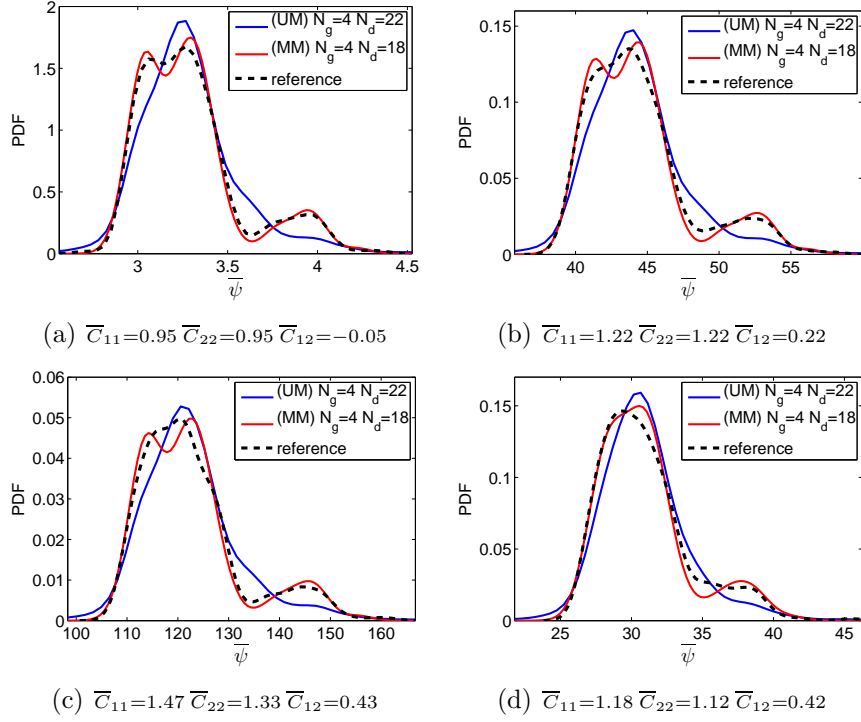


Figure 15: PDFs of  $\bar{\Psi}(\bar{C})$  computed with strategies (UM), (MM) and the reference solution; (a) large scale strain state (v); (b) large scale strain state (vi); (c) large scale strain state (vii); (d) large scale strain state (viii).

and 17 respectively illustrate the PDFs of quantities  $\bar{\Psi}$ ,  $\bar{S}_{11}$  and  $\bar{L}_{1111}$  for strain states (v) to (viii). We can first notice that, as previously, strategy (MM) leads to better results than strategy (UM). Then, we can observe that the results are very good for  $\psi$ , but slightly deteriorating for components of  $\bar{S}$  and a little more for components of  $\bar{L}$ . However, results obtained with strategy (MM) remain completely acceptable. A simple way to improve the results would be to increase the number  $Q$  of components in vector  $\bar{\Psi}$ , that is to say to refine the discretization of the large scale strain space. However, this action would increase the CPU times required to compute the numerical database.

### 6.3. Application 3: large scale structural problem

In this example, we propose to study the efficiency of the proposed approach with a large scale structural problem. The aim is to compare the

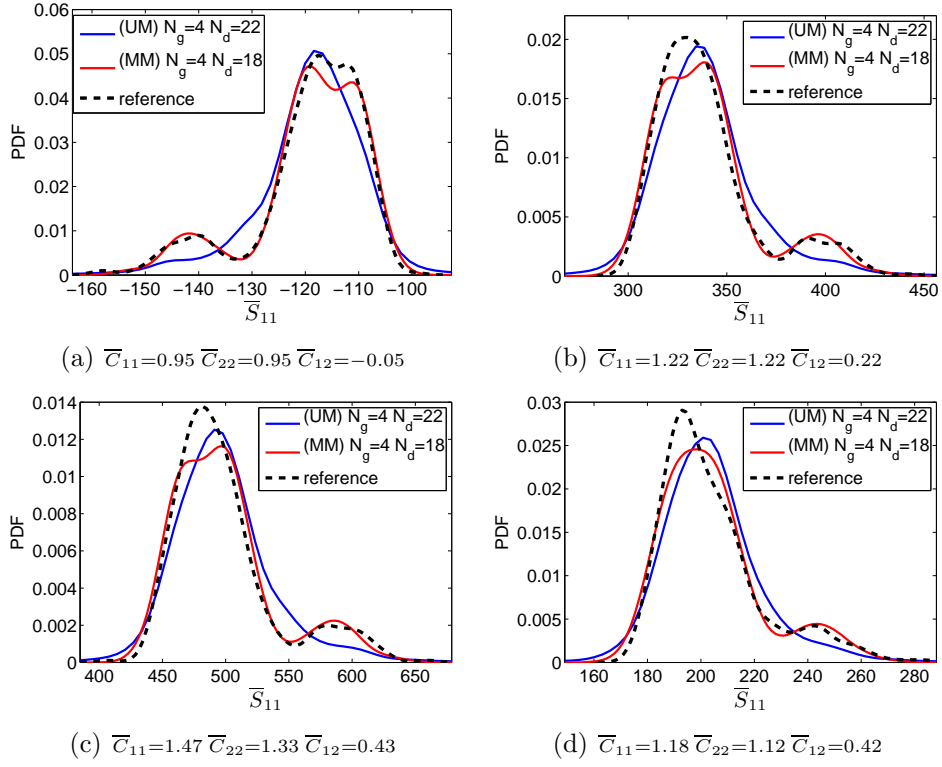


Figure 16: PDFs of component  $\bar{S}_{11}(\bar{C})$  computed with strategies (UM), (MM) and the reference solution; (a) large scale strain state (v); (b) large scale strain state (vi); (c) large scale strain state (vii); (d) large scale strain state (viii)

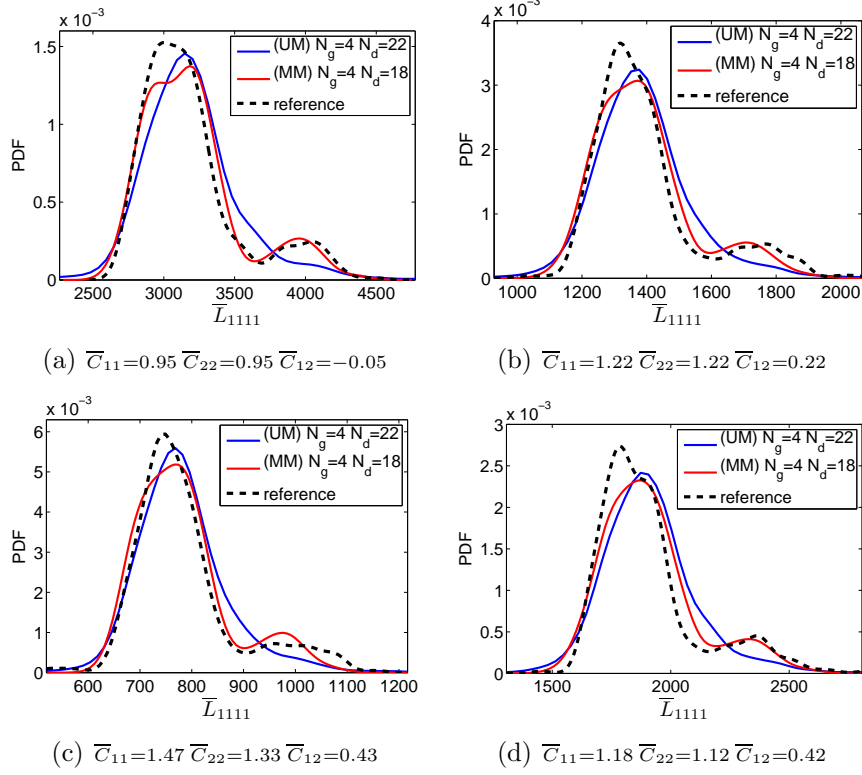


Figure 17: PDFs of component  $\bar{L}_{1111}(\bar{C})$  computed with strategies (UM), (MM) and the reference solution; (a) large scale strain state (v); (b) large scale strain state (vi); (c) large scale strain state (vii); (d) large scale strain state (viii)

results obtained with the different strategies ((UM) and (MM)) proposed for the stochastic representation of the apparent constitutive equations and discussed in Sec. 6.2.

### 6.3.1. Problem definition

We consider a structure made of a hyperelastic heterogeneous material where the geometry of the microstructure associated to the material is random. At the small scale, the length of the square plate is  $l = 10^{-3}$  m. At the large scale, the dimensions of the structure lying in a domain  $\overline{\Omega}$  are  $L = 0.1$  m,  $H = 0.1$  m and  $e = 0.02$  m and displacements  $\Delta_{\underline{u}} = 10\%$  are imposed on a part  $\overline{\Gamma_{\underline{u}}}$  of the structural domain presented on Fig. 18(a). The mesh of the mesoscopic domain is composed of 372 3-nodes triangular finite elements depicted on Fig. 18(b). The small scale problem corresponds to the one studied in Section 6.2 and the apparent constitutive behavior is characterized by the apparent strain energy density functions determined with strategies (UM) and (MM) for which the identification on the polynomial chaos leads to the better approximation according to the  $L^1$ -log error function (30). In [7], the properties of the random field generated by the proposed stochastic model of the microstructure has been studied by the authors which have shown that the spatial correlation length is 7 times superior to the size of the elementary cell which explains the statistical fluctuations observed in the previous study of  $\overline{\Psi}$ . Considering the dimensions of the problem, the distance of two integration points at the large scale is superior to the spatial correlation length. Thus, the large scale problem is a mesoscopic problem for which the apparent quantities still present stochastic fluctuations. During the mesoscopic computation, integration points must be associated with a microstructure, represented by a potential  $\overline{\Psi}$ , which corresponds to independent realizations of  $\overline{\Psi}$  generated with its polynomial chaos representation.

### 6.3.2. Results

In this section, we propose to analyze the statistical properties of several mesoscopic quantities. To achieve this, we run  $\mu_{meso} = 1,000$  Monte-Carlo simulations of the structural problem for each characterization of the apparent strain energy density function related to the identification strategies. A reference solution is computed consisting in relating a novel realization of  $\overline{\Psi}$  to each integration point generated with the random generator presented in Sec. 3 for which a separated variables representation is then calculated. Those numerical simulations can be summarized in three steps: (i)

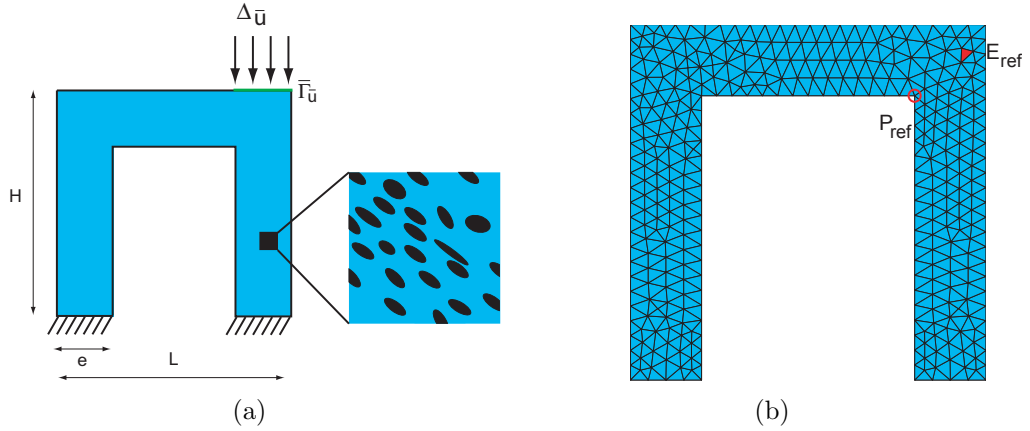


Figure 18: (a): Geometry and boundary conditions for the large scale structural problem; (b): Finite element mesh associated with the microstructure.

using the random generator to get new realizations of the geometry of the microstructure associated with each integration point; *(ii)* using the deterministic NEXP approach to determine an explicit form of the potential with respect to the large scale strains; *(iii)* compute the large scale response with nonlinear FEM simulations. In this procedure, step *(ii)* is very expensive since a full NEXP strategy is used for each integration point. Indeed, the proposed methodology allows performing one large scale simulation with a laptop computer in less than an hour, when it takes around two days with the reference solution.

One should note that this procedure is very expensive in terms of computational times because of the independent generations of vector  $\bar{\Psi}$ . As an illustration of the mesoscopic numerical simulations, Fig. 19 presents the von Mises stress fields  $\bar{\sigma}_{eq}$  for two different cases of applied displacements corresponding to  $\Delta \bar{u}_1 = 5\%$  and  $\Delta \bar{u}_2 = 10\%$  for a particular realization of the mesoscopic structure. We clearly observe two areas where the stresses are concentrated located on the right side of the structure where the displacements are imposed.

We first focus on the mesoscopic von Mises stress  $\bar{\sigma}_{eq}$  for a particular finite element  $E_{elem}$  depicted in Fig. 18(b). Fig. 20 illustrates the convergence of the mean and standard deviation of  $\bar{\sigma}_{eq}$  for  $E_{elem}$  according to the number of realizations as well as the probability density functions corresponding to the different identifications strategies. From this figure, it appears that running

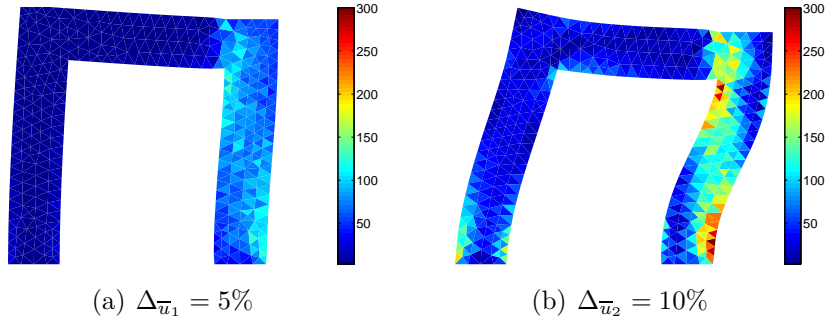


Figure 19: Stress fields  $\bar{\sigma}_{eq}$  for one particular mesoscopic simulation; (a): solution corresponding to imposed displacements  $\Delta_{\bar{u}_1} = 5\%$ ; (b) solution corresponding to imposed displacements  $\Delta_{\bar{u}_2} = 10\%$ .

$\mu_{meso} = 1000$  Monte-Carlo simulations yields to reasonably converged results in terms of mean and standard deviation of  $\bar{\sigma}_{eq}$ . As we can deduce from the various PDFs,  $\bar{\sigma}_{eq}$  for  $E_{elem}$  still presents statistical fluctuations: coefficients of variation are indeed of 15.7% and 16.2% respectively for strategies (UM) and (MM) while the coefficient of variation for the reference solution is equal to 16.4%. Surprisingly, the two identification strategies lead to similar results which appear acceptable comparing to the reference solution. However, we can notice that strategy (MM) leads to the best results for the probability density functions since the two modes, appearing in the reference solution, are well captured by this strategy.

We then focus on the maximum of the von Mises stresses defined as  $\bar{\sigma}_{eq}^{max} = \max_{\mathbf{x} \in \bar{\Omega}} |\bar{\sigma}_{eq}(\mathbf{x})|$ . Fig. 21 illustrates the convergence of the mean and standard deviation of  $\bar{\sigma}_{eq}^{max}$  according to the number of realizations as well as the probability density functions of  $\bar{\sigma}_{eq}^{max}$  corresponding to the different identifications strategies. We also notice a good agreement between the two strategies and the reference solution and, here again, strategy (MM) seems to lead to the best results for the probability density functions. Moreover, results coming from strategy (UM) are very acceptable even if this strategy has led to a coarse identification of the apparent strain energy density function (*c.f.* results shown in Sec. 6.2).

We then focus on the horizontal displacement  $u_x(P_{ref})$  of point  $P_{ref}$  depicted on figure 18(b). Fig. 22 illustrates the evolution of component  $u_x(P_{ref})$  according to the displacements  $\Delta_{\bar{u}}$  applied to the part  $\bar{\Gamma}_{\bar{u}}$  of the boundary and

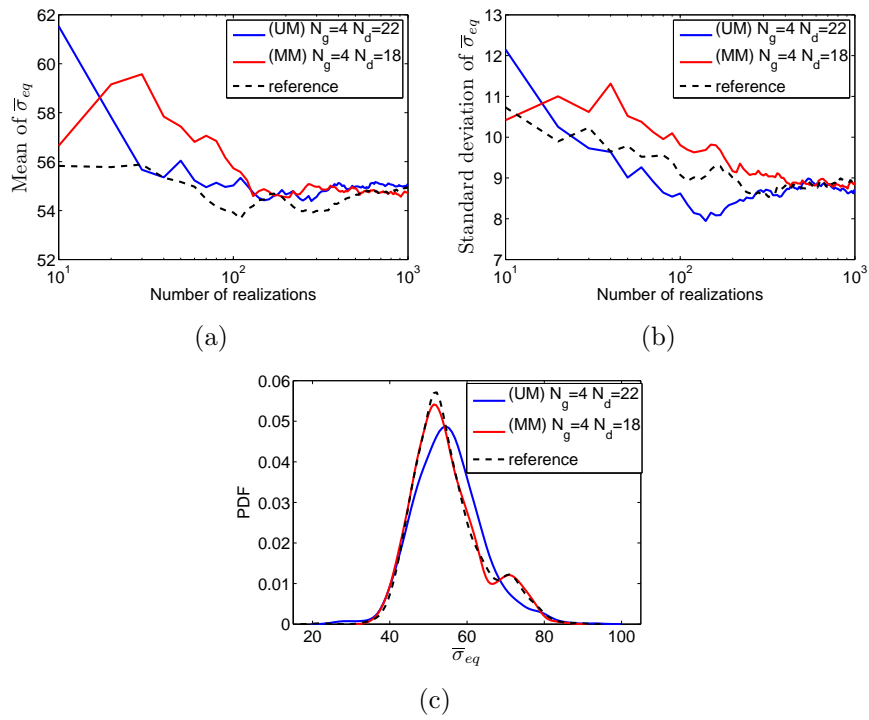


Figure 20: (a) and (b): Convergence of mean and standard deviation of  $\bar{\sigma}_{eq}$  for  $E_{elem}$ , computed with strategies (UM), (MM) and the reference solution, according to the number of Monte-Carlo simulations; (c): Pdfs of  $\bar{\sigma}_{eq}$  for  $E_{elem}$ .

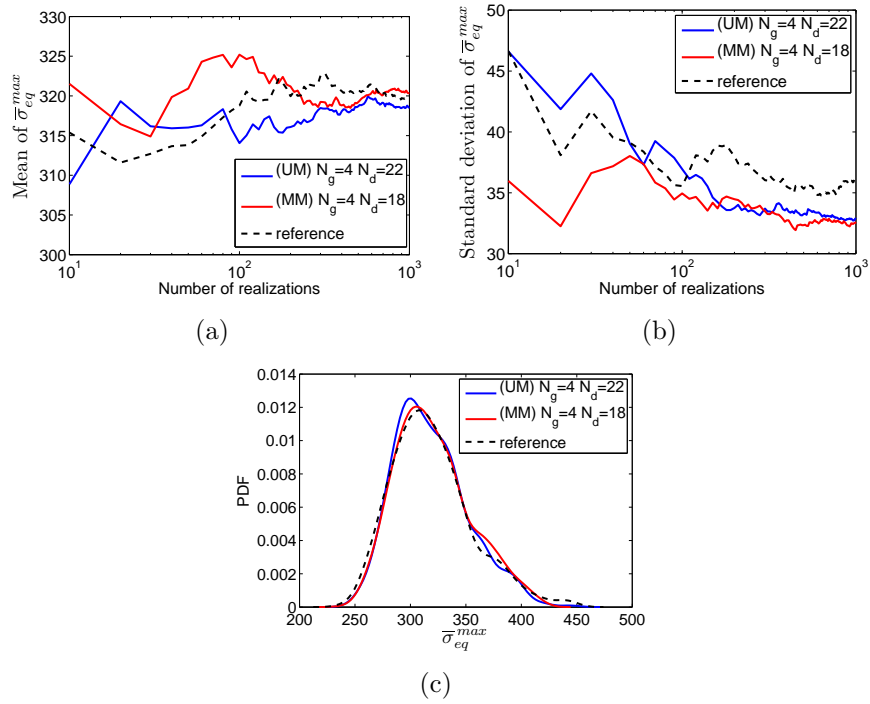


Figure 21: (a) and (b): Convergence of mean and standard deviation of  $\bar{\sigma}_{eq}^{max}$ , computed with strategies (UM), (MM) and the reference solution, according to the number of Monte-Carlo simulations; (c) PDFs of  $\bar{\sigma}_{eq}^{max}$ .

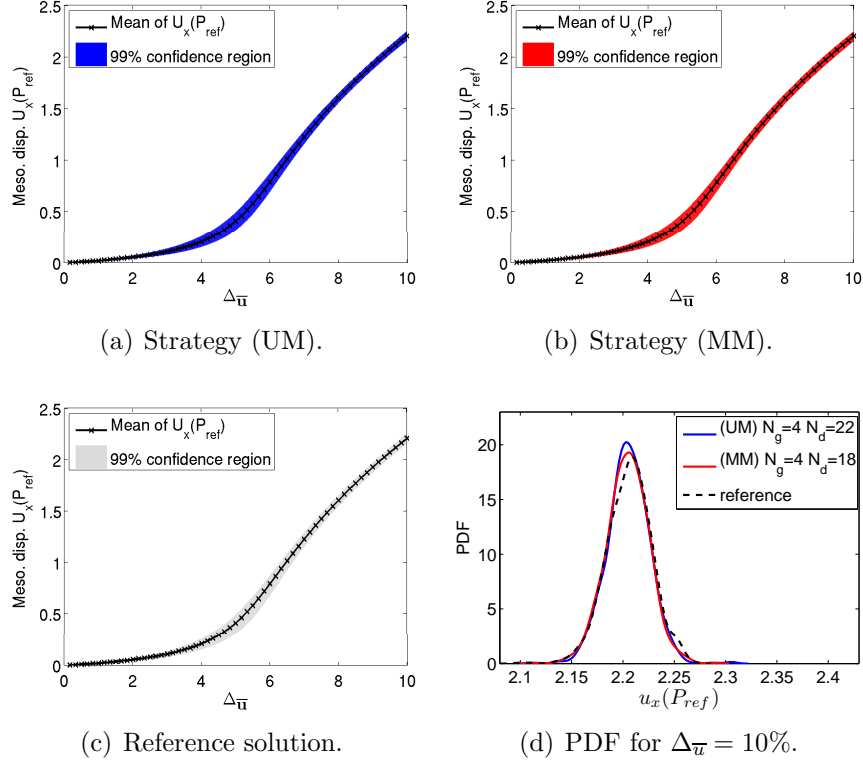


Figure 22: (a) to (c): Evolution of component  $u_x$  of displacement at point  $P_{ref}$  according to  $\Delta_{\bar{u}}$  computed with strategies (UM), (MM) and the reference solution; (d) PDFs of  $u_x$  at point  $P_{ref}$  corresponding to  $\Delta_{\bar{u}} = 10\%$ .

corresponding to the different identification strategies and the reference solution. We can observe that all the solutions match the reference solution for both linear and nonlinear parts of the response surfaces. On Fig. 22 are also plotted the PDFs of each solution corresponding to the maximum imposed displacements which are very similar and also close to the reference PDF. Finally we can notice that the statistic fluctuations are very low allowing considering the displacements as a deterministic quantity: indeed, the coefficient of variation of  $u_x(P_{ref})$  is equal to 0.9% for both strategies (UM) and (MM) when the coefficient of variation of the reference solution is 1%. This is mainly due to the Dirichlet boundary conditions applied on the mesoscopic structure.

We finally focus on an integrated quantity linked to the mesoscopic stress

field. We introduce the mesoscopic resultant force  $\overline{\mathbf{F}}$  computed on the boundary  $\Gamma_{\overline{u}}$  according to the following relationship

$$\overline{\mathbf{F}} = \int_{\Gamma_{\overline{u}}} \overline{\mathbf{P}} \widehat{\mathbf{N}} d\Gamma. \quad (31)$$

where  $\widehat{\mathbf{N}}$  is the outward unit normal vector to the boundary  $\partial\overline{\Omega}$ . The component  $\overline{F}_y$  of  $\overline{\mathbf{F}}$  for the mesoscopic structure with respect to the applied displacements  $\Delta_{\overline{u}}$  is depicted on Fig. 23 for the different identification strategies and the reference solution. As for the displacement  $u_x(P_{ref})$ , we can observe a very good match between all the results in comparison of the reference solution. Moreover, we notice that the stochastic fluctuations increase according to the applied displacements  $\Delta_{\overline{u}}$  leading to coefficients of variation corresponding to  $\Delta_{\overline{u}} = 10\%$  equal to 4.8% and 5.2% respectively for strategies (UM) and (MM). Those results also match the reference solution whose coefficient of variation is equal to 4.9%. As opposed to the horizontal displacements showing on Fig. 22, the resultant force presents significant statistic fluctuations directly related to the statistic fluctuations of the apparent strain energy density function. Once again, strategy (UM), which has led to coarse results shown in Sec. 6.2, presents satisfying performances for the mesoscopic problem.

## 7. Conclusion

We have proposed a novel approach dedicated to the approximation of random apparent (or effective) constitutive equations for hyperelastic heterogeneous microstructures. This work is an extension to the stochastic framework of a non-concurrent computational homogenization approach called the Numerical EXplicit Potential method (NEXP) which consists in characterizing the effective constitutive behavior by an explicit continuous form of the effective strain energy density function (potential). Such a form simply allows obtaining the large scale (mesoscopic or macroscopic) tensors, needed in a structural analysis, by derivation of the potential. In a recent work by the authors [7], this methodology has been extended to the stochastic case but greatly suffers from the ‘‘curse of dimensionality’’ since a high number of random parameters involves drastic computational times.

To circumvent this difficulty, we have proposed a reformulation of the problem leading us to the identification of the apparent (or effective) potential

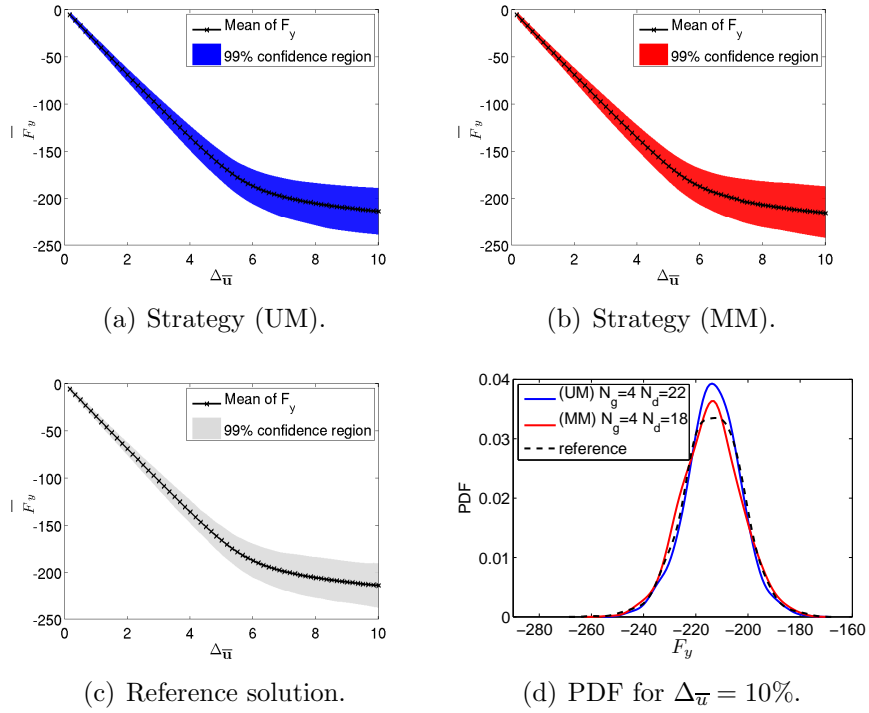


Figure 23: (a) to (c): Evolution of component  $\bar{F}_y$  of the resultant force  $\bar{\mathbf{F}}$  according to  $\Delta_{\bar{u}}$  computed with strategies (UM), (MM) and the reference solution; (d): PDFs of  $\bar{F}_y$  corresponding to  $\Delta_{\bar{u}} = 10\%$ .

represented on a polynomial chaos expansion. We have considered fiber reinforced polymer composites for which the geometry of the microstructure is random and is governed by a high number of random parameters. Using a specific random generator of microstructures, which can be replaced by any other generator with the same capabilities, we use the deterministic NEXP method to compute realizations of the strain energy density function for prescribed mesoscopic (or macroscopic) scale strain states. Starting from this numerical database, a statistical reduction of the discretized potential is performed and the reduced-order random variables are identified on polynomial chaos expansions. Once the identification on the polynomial chaos of the apparent potential is done, the explicit continuous form of each realization of the apparent potential, generated from its polynomial chaos expansion, is easily obtained thanks to a separated variables representation coupled to an appropriate interpolation scheme.

In this work, the main difficulty comes from the identification of the apparent (or effective) potential on polynomial chaos expansions which is not a trivial task since a high number of coefficients may be needed in the polynomial chaos expansion. We have thus used the novel identification technique proposed and successfully employed in [39, 41]. In a first numerical example, for which the random parameters to be identified were uni-modal random variables, this technique has led us to very satisfying results. However, in a second example, we have shown that the random apparent potential may be of multi-modal nature which increases the difficulty of the problem since a high order of the polynomial chaos is needed to well represent such random variables. To circumvent this difficulty, we have proposed to use a prior stochastic model based on mixture of polynomial chaos. This prior stochastic model has allowed improving the identification procedure without increasing the order of the polynomial chaos expansions and thus, has prevented from increasing the computational costs. Finally, a third numerical example consisting in a mesoscopic problem has been proposed to show the usefulness and the efficiency of the approach. In this illustration, the two identification strategies have been used to characterize the apparent constitutive equations and their performances have been compared. Surprisingly, the two strategies have both led to good results regarding the reference solution, whereas the identification strategy not based on the mixture of polynomial chaos had led to a rather poor identification of the apparent constitutive potential.

## 8. Acknowledgements

This research was funded by the French Research Agency (Agence Nationale de la Recherche) under TYCHE contract ANR-2010-BLAN-0904.

## References

- [1] J. Aboudi, Finite strain micromechanical modeling of multiphase composites, *International Journal of Multiscale Computational Engineering*, 6(5) (2008) 411-434.
- [2] M. Arnst, R. Ghanem, C. Soize, Identification of Bayesian posteriors for coefficients of chaos expansion, *Journal of Computational Physics*, 229(9) (2010) 3134-3154.
- [3] I. Babuska, R. Tempone, G.E. Zouraris, Solving elliptic boundary value problems with uncertain coefficients by the finite element method: the stochastic formulation, *Computer Methods in Applied Mechanics and Engineering* 194(12-16) (2005) 1251-1294.
- [4] Z.I. Botev, J.F. Grotowski, D.P. Kroese, Kernel density estimation via diffusion, *The Annals of Statistics*, 38(5) (2010) 2916-2957.
- [5] A.W. Bowman, A. Azzalini, *Applied Smoothing Techniques for Data Analysis*, Oxford University Press, 1997.
- [6] J.D. Carol, J.J. Chang, Analysis of individual differences in multidimensional scaling via an N-way generalization of 'Eckart-Young' decomposition, *Psychometrika*, 35 (1970) 283-319.
- [7] A. Clément, C. Soize, J. Yvonnet, Computational nonlinear stochastic homogenization using a non-concurrent multiscale approach for hyperelastic heterogeneous microstructures analysis, *International Journal for Numerical Methods in Engineering*, 91(8) (2012) 799824.
- [8] G. deBotton, G. Shmuel, A new variational estimate for the effective response of hyperelastic composites, *Journal of the Mechanics and Physics of Solids*, 58(4) (2010) 466-483.
- [9] C. Desceliers, R. Ghanem, C. Soize, Maximum likelihood estimation of stochastic chaos representations from experimental data, *International Journal for Numerical Methods in Engineering*, 66(6) (2006) 978-1001.

- [10] C. Desceliers, C. Soize, R. Ghanem, Identification of chaos representations of elastic properties of random media using experimental vibration tests, *Computational Mechanics*, 39(6) (2007) 831-838.
- [11] A. Doostan, H. Owhadi, A non-adapted sparse approximation of PDEs with stochastic inputs, *Journal of Computational Physics*, 230 (2011) 3015-3034.
- [12] F. Feyel, J.L. Chaboche, FE2 multiscale approach for modelling the elastoviscoplastic behaviour of long fiber SiC/Ti composite materials, *Computer Methods in Applied Mechanics and Engineering*, 183 (2000), 309-330.
- [13] B. Ganapathysubramanian, N. Zabaras, Sparse grid collocation schemes for stochastic natural convection problems, *Journal of Computational Physics*, 225 (2007) 652-685.
- [14] R. Ghanem, P.D. Spanos, *Stochastic Finite Elements: A spectral Approach*, Spinger-verlag, New-York, 1991 (revised edition, Dover Publications, New York, 2003).
- [15] R. Ghanem, R.M. Kruger, Numerical solution of spectral stochastic finite element system, *Computer Methods in Applied Mechanics and Engineering*, 129 (1996), 289-303.
- [16] R. Ghanem, Ingredients for a general purpose stochastic finite elements implementation, *Computer Methods in Applied Mechanics and Engineering*, 168 (1999), 19-34.
- [17] R. Ghanem, A. Doostan, On the construction and analysis of stochastic models; characterization and propagation of the errors associated with limited data, *Journal of Computational Physics*, 217 (2006) 63-81.
- [18] J. Guilleminot, C. Soize, D. Kondo, Mesoscale probabilistic model for the elasticity tensor of fiber reinforced composites: Experimental identification and numerical aspects, *Mechanics of Materials*, 41 (2009) 1309-1322.
- [19] B. Hiriyur, H. Waisman, G. Deodatis, Uncertainty quantification in homogenization of heterogeneous microstructures modeled by XFEM, *International Journal of Numerical Methods in Engineering*, 86 (2011) 257-278.

- [20] G. Holzapfel, *Nonlinear Solid Mechanics: A Continuum Approach for Engineering*, John Wiley and Sons, Chichester, 2000.
- [21] H.A.L. Kiers, Toward a standardized notation and terminology in multiway analysis, *Journal of Chemometrics*, 14 (2000) 105-122.
- [22] O.M. Knio, O.P. Le Maitre, Uncertainty propagation in CFD using polynomial chaos decomposition, *Fluid Dynamics Research* 38(9) (2006) 616-640.
- [23] O.P. Le-Maitre, O.M. Knio, *Spectral Methods for Uncertainty Quantification with Applications to Computational Fluid Dynamics*, Springer, Heidelberg, 2010.
- [24] O.P. Le-Maitre, O.M. Knio, H.J. Najm, R.G. Ghanem, Uncertainty propagation using Wiener-Haar expansions; *Journal of Computational Physics*, 197 (2004) 28-57.
- [25] M. Loève, *Probability Theory. I*, fourth edition, in: *Graduate Texts in Mathematics*, vol. 45, Springer-Verlag, New-York, 1977.
- [26] O. Lopez-Pamies, P. Ponte Castañeda, Second-Order Estimates for the Macroscopic Response and Loss of Ellipticity in Porous Rubbers at Large Deformations, *Journal of Elasticity*, 76 (2004) 247-287.
- [27] E. Monteiro, J. Yvonnet, Q.C. He, Computational Homogenization for nonlinear conduction in heterogeneous materials using model reduction, *Computational Materials Science*, 42 (2008) 704-712.
- [28] S. Nezamabadi, J. Yvonnet, H. Zahrouni, M. Pottier-Ferry, A multilevel computational strategy for handling microscopic and macroscopic instabilities, *Computer Methods in Applied Mechanics and Engineering*, 198 (2009) 2099-2110.
- [29] A. Nouy, O. P. Le Maître, Generalized spectral decomposition for stochastic nonlinear problems, *Journal of Computational Physics*, 228(1) 2009 202-235.
- [30] A. Nouy, Identifications of multi-modal random variables through mixtures of polynomial chaos expansions, *Comptes Rendus Mécanique*, 338(12) (2010) 698-703.

- [31] A. Nouy, M. Chevreuril, E. Safatly, Fictitious domain method and separated representations for the solution of boundary value problems on uncertain parameterized domains, *Computer Methods in Applied Mechanics and Engineering*, 200 (2011) 3066-3082.
- [32] A. Nouy, A. Clément, An eXtended Stochastic Finite Element Method for the numerical simulation of random multi-phased materials, *International Journal for Numerical Methods in Engineering*, 83 (2010) 1312-1344.
- [33] R.W. Ogden, G. Saccomandi, I. Sgura, Fitting hyperelastic models to experimental data, *Computational Mechanics*, 34 (2004) 484-502.
- [34] P. Ponte-Castañeda, E. Tiberio, Second-order homogenization method in finite elasticity and applications to black-filled elastomers, *Journal of the Mechanics and Physics of Solids*, 48(6-7) 2000 1389-1411.
- [35] G.I. Schueller, On the treatment of uncertainties in structural mechanics and analysis, *Computers and Structures* 85(5) (2007) 235-243.
- [36] R. J. Serfling, *Approximation Theorems of Mathematical Statistics*, John Wiley & Sons, 1980.
- [37] R. Smit, W. Brekelmans, H. Meijer, Prediction of the mechanical behavior of nonlinear heterogeneous systems by multi-level finite element modeling, *Computer Methods in Applied Mechanics and Engineering*, 155 (1998) 181-192.
- [38] C. Soize, Generalized probabilistic approach of uncertainties in computational dynamics using random matrices and polynomial chaos decompositions, *International Journal for Numerical Methods in Engineering* 81(8) (2010) 939-970.
- [39] C. Soize, Identification of high-dimension polynomial chaos expansions with random coefficients for non-Gaussian tensor-valued random fields using partial and limited experimental data, *Computer Methods in Applied Mechanics and Engineering*, 199(33-36) (2010) 2150-2164.
- [40] C. Soize, C. Desceliers, Computational aspects for constructing realizations of polynomial chaos in high dimension, *SIAM Journal on Scientific Computing*, 32(5) (2010) 2820-2831.

- [41] C. Soize, A computational inverse method for identification of non-Gaussian random fields using the bayesian approach in very high dimension, *Computer Methods in Applied Mechanics and Engineering*, 200 (2011) 3083-3099.
- [42] J.C. Spall, *Introduction to Stochastic Search and Optimization*, John Wiley and Sons, Hoboken, New Jersey, 2003.
- [43] G. Stefanou, A. Nouy, A. Clément, Identification of random shapes from images through polynomial chaos expansion of random level-set functions, *International Journal for Numerical Methods in Engineering* 79 (2009) 127-155.
- [44] N. Takano, M. Zako, Y. Ohnishi, Macro-micro uncoupled homogenization procedure for microscopic nonlinear behavior analysis of composites, *Materials science research international*, 2(2) (1996) 81-86.
- [45] I. Temizer, P. Wriggers, An adaptive method for homogenization in orthotropic nonlinear elasticity, *Computer Methods in Applied Mechanics and Engineering*, 35-36 (2007) 3409-3423.
- [46] K. Terada, N. Kikuchi, A class of general algorithms for multi-scale analysis of heterogeneous media, *Computer Methods in Applied Mechanics and Engineering*, 190 (2001) 5427-5464.
- [47] M. Tootkaboni, L. Graham-Brady, A Multi-scale spectral stochastic method for homogenization of multi-phase periodic composites with random material properties, *International Journal of Numerical Methods in Engineering*, 83 (2010) 59-90.
- [48] S. Torquato, *Random Heterogeneous Materials: Microstructures and Macroscopic Properties*, Springer, New-York, 2002.
- [49] J. Yvonnet, Q.C. He, The Reduced Model Multiscale Method (R3M) for the nonlinear homogenization of hyperelastic media at finite strains, *Journal of Computational Physics*, 223 (2007) 341-368.
- [50] J. Yvonnet, D. Gonzalez, Q.C. He, Numerically explicit potentials for the homogenization of nonlinear elastic heterogeneous materials, *Computer Methods in Applied Mechanics and Engineering*, 198 (2009) 2723-2737.

- [51] J. Yvonnet, Q.C. He, A non-concurrent multiscale method for computing the response of nonlinear elastic heterogeneous structures, *European Journal of Computational Mechanics* 19 (2010) 105-116.
- [52] J. Yvonnet, E. Monteiro, Q.C. He, Computational homogenization of hyperelastic heterogeneous structures: a non-concurrent approach, submitted for publication.
- [53] T. Zhang, G.H. Golub, Rank-one approximation to high order tensor, *SIAM Journal of Matrix Analysis and Applications*, 23(2) (2001) 534-550.